JOURNAL OF PETROLOGY | VOLUME 48 | NUMBER 11 | PAGES 2033–2061 | 2007 | doi:10.1093/petrology/egm049

Adakitic Dacites Formed by Intracrustal Crystal Fractionation of Water-rich Parent Magmas at Nevado de Longaví Volcano (36·2°S; Andean Southern Volcanic Zone, Central Chile)

CAROLINA RODRÍGUEZ[1,2], DANIEL SELLÉS[1,2]*, MICHAEL DUNGAN[1], CHARLES LANGMUIR[2] AND WILLIAM LEEMAN[3]

[1]UNIVERSITÉ DE GENÈVE, DÉPARTEMENT DE MINÉRALOGIE, 13 RUE DES MARAICHERS, 1205 GENEVA, SWITZERLAND

[2]DEPARTMENT OF EARTH AND PLANETARY SCIENCES, HARVARD UNIVERSITY, 20 OXFORD STREET, CAMBRIDGE, MA 02138, USA

[3]NATIONAL SCIENCE FOUNDATION, 4201 WILSON BLVD., ARLINGTON, VA 22230, USA

RECEIVED SEPTEMBER 22, 2006; ACCEPTED JULY 31, 2007
ADVANCE ACCESS PUBLICATION OCTOBER 8, 2007

The mid-Holocene eruptive products of Nevado de Longaví volcano (36·2°S, Chile) are the only reported occurrence of adakitic volcanic rocks in the Quaternary Andean Southern Volcanic Zone (33–46°S). Dacites of this volcano are chemically distinct from other evolved magmas of the region in that they have high La/Yb (15–20) and Sr/Y (60–90) ratios and systematically lower incompatible element contents. An origin by partial melting of high-pressure crustal sources seems unlikely from isotopic and trace element considerations. Mafic enclaves quenched into one of the dacites, on the other hand, constitute plausible parental magmas. Dacites and mafic enclaves share several characteristics such as mineral chemistry, whole-rock isotope and trace element ratios, highly oxidizing conditions (NNO + 1·5 to >NNO + 2, where NNO is the nickel–nickel oxide buffer), and elevated boron contents. A two-stage mass-balance crystal fractionation model that matches both major and trace elements is proposed to explain magmatic evolution from the least evolved mafic enclave to the dacites. Amphibole is the main ferromagnesian phase in both stages of this model, in agreement with the mineralogy of the magmas. We also describe cumulate-textured xenoliths that correspond very closely to the solid assemblages predicted by the model. We conclude that Nevado de Longaví adakitic dacites are the products of polybaric fractional crystallization from exceptionally water-rich parent magmas. These basaltic magmas are inferred to be related to an exceptionally high, but transient input of slab-derived fluids released from serpentinite bodies hosted in the oceanic Mocha Fracture Zone, which projects beneath Nevado de Longaví. Fractional crystallization that is modally dominated by amphibole, with very minor garnet extraction, is a mechanism for generating adakitic magmas in cold subduction zones where a high flux of slab-derived fluids is present.

KEY WORDS: *adakite; amphibole; Andes; differentiation; Southern Volcanic Zone*

INTRODUCTION

Most of the magmatism at convergent plate margins originates in the high-temperature region of the asthenospheric mantle wedge as a consequence of fluxing by fluids liberated from subducted oceanic crust. Erupted magmas derived directly by melting of the oceanic crust are rare for a number of reasons. Foremost among these is that most thermal models require subduction of late Miocene or younger oceanic lithosphere to reach the temperature of the wet basaltic solidus at depths of 90–120 km (e.g. Peacock & Wang, 1999). By defining the geochemical characteristics of arc magmas presumed to be products of slab melting (elevated La/Yb, elevated Sr and Al_2O_3 contents, and high Sr/Y) and then giving this magma type the name 'adakite' (following Kay, 1978), Defant & Drummond (1990) have created a serious nomenclatural

*Corresponding author. Present address: Department of Earth and Planetary Sciences, Harvard University, 20 Oxford Street, Cambridge, MA 02138, USA. E-mail: dselles@fas.harvard.edu

problem; that is, a rock's name and its definition are tied to a particular interpretation of its magmatic genesis, thereby tainting the meaning of the term adakite when it is applied to all magmas that have the requisite chemical signature, regardless of their origin. We use the rock name 'adakite' with these caveats in mind, and only in the sense of a magma that has specific chemical characteristics.

There are a number of documented examples of adakitic magmas in subduction settings that do not conform to the thermal requirements associated with subduction of very young oceanic lithosphere. Some of these occurrences have been explained in terms of special geodynamic circumstances, such as subduction of a slab edge or slab-window (Sajona *et al.*, 1993; Yogodzinski *et al.*, 2001; Thorkelson & Breitsprecher, 2005), highly oblique convergence (Yogodzinski & Kelemen, 1998), and flat subduction (Gutscher *et al.*, 2000). Other high-pressure crustal metabasaltic reservoirs, such as mafic mantle-derived material underplated at the base of thickened orogenic crust (e.g. Atherton & Petford, 1993, 1996) or tectonically eroded lower forearc crust slivers subducted beneath the arc (Kay *et al.*, 2005; Goss & Kay, 2006) have been proposed as alternative sources to the oceanic crust to explain adakites in cold subduction settings. Although some of these interpretations remain controversial, the feature that all of these occurrences have in common is that the adakitic elemental signature requires sufficiently high pressures and water contents to stabilize residual garnet ± hornblende and to significantly suppress residual plagioclase. Crystal fractionation of the requisite mineral assemblage from wet basaltic magmas also may produce evolved magmas with adakitic chemical characteristics (Castillo *et al.*, 1999; Kleinhanns *et al.*, 2003; Prouteau & Scaillet, 2003; Castillo, 2006; Macpherson *et al.*, 2006).

The topic of this paper is the only case of Quaternary adakitic magmas in the Andean Southern Volcanic Zone (SVZ). We report mineral and whole-rock chemistry for Nevado de Longaví volcano (NLV) magmas, with an emphasis on Holocene adakitic dacites (mainly pyroclastic rocks), their quenched magmatic enclaves, and hornblende-rich cumulate-textured xenoliths. The generation of adakitic magmas at NLV appears to be disconnected from factors such as crustal thickness and character that dominate in most of the along-arc trends defined by other SVZ frontal arc volcanoes, and we postulate that the highly localized occurrence of these magmas is linked in space and time to subduction of the oceanic Mocha Fracture Zone. We propose a model that reproduces the major and trace element compositions of adakitic dacites from plausible mafic precursors, wherein the adakitic signature is ascribed to two-stage, polybaric intra-crustal crystal fractionation of exceptionally water-rich mantle-derived mafic melts, without a contribution from slab melting.

TECTONIC SETTING

Nevado de Longaví volcano (NLV: 36·2°S) lies on the front of the Andean Southern Volcanic Zone (SVZ: 33–46°S), which is the product of subduction of the Nazca plate beneath the South American plate (Fig. 1). The Quaternary frontal arc of the SVZ records large along-arc changes in evolved magma compositions and variable proportions of mafic to silicic magmas at these edifices (Hickey *et al.*, 1986; Hildreth & Moorbath, 1988; Tormey *et al.*, 1991). Two key observations from recent work are that the latitude of 36–36·2°S separates the SVZ into two contrasting magmatic domains and that these differences correlate with regional trends in the character and thickness of the crust underlying the arc. The mean elevation of the Andean Cordillera and the summit altitudes of frontal arc edifices increase progressively to the north of NLV by more than 2000 m, and crustal thickness inferred from an increasingly negative Bouguer gravity anomaly (Tassara & Yañez, 2003; Tassara, 2005) may increase by as much as 30 km. These parameters decrease to the south of NLV, where the arc lies near the western boundary of the Andean Cordillera, but with lower gradients than are observed to the north. This is in part due to the fact that the strike of the arc changes at ~36°S from oblique to the Andean axis north of NLV (toward the Andean crest) to trench-parallel south of this latitude. The crustal thickness at the northern end of the SVZ (33–34·5°S) is inferred to be ~60–55 km, whereas at 42°S it might be <30 km. The sub-arc crust at the latitude of NLV is probably ~35–40 km thick (Tassara & Yañez, 2003; Tassara, 2005). These changes in along-strike crustal thickness are related to changes in the style and timing of compressive deformation in the foreland that also coincides with 36–37°S (Ramos *et al.*, 1996; Kley & Monaldi, 1998; Kley *et al.*, 1999; Ramos, 1999; Folguera *et al.*, 2002, 2004).

The position of NLV is coincident with the projection of the oceanic Mocha Fracture Zone beneath the Quaternary arc (after correction for a subduction dip angle of 30°, Bohm *et al.*, 2002), which at the trench separates 35 Ma oceanic crust to the north from younger crust (~25 Ma) to the south (Tebbens & Cande, 1997). The N60°E-trending Mocha Fracture Zone is oblique to the N80°E convergence vector of the Nazca plate (Fig. 1) and it has been migrating southward along the arc at a rate of ~30 km/Myr.

The whole-rock chemistry and characteristic mineral assemblages of magmas change along the SVZ, as do the lithologies, age, and thickness of the underlying crust. Volcanoes located at the northern end of the SVZ (33–34·5°S), where the crust is thickest, have emitted dominantly andesitic and more silicic lavas characterized by isotopic ratios and trace element abundances indicative

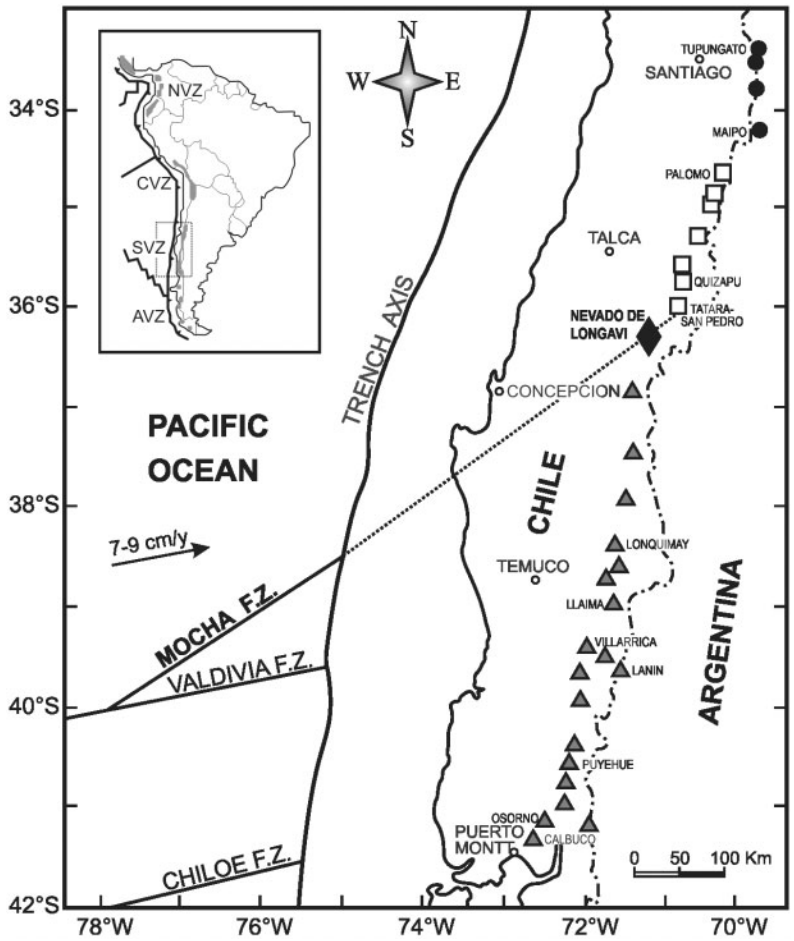

Fig. 1. Location of Nevado de Longaví volcano (black diamond) and other volcanic centers of the Southern Volcanic Zone (SVZ). Inset shows the position of the SVZ relative to the Northern, Central, and Austral Volcanic zones (NVZ, CVZ, and AVZ, respectively). Different symbols represent the segmentation scheme (Dungan *et al.*, 2001; Sellés *et al.*, 2004): Tupungato–Maipo segment (circles); Palomo–Tatara segment (squares) and Nevado de Longaví–Osorno segment (triangles). Oceanic fracture zones after Herron (1981) and Tebbens & Cande (1997). The landward projection of the Mocha Fracture Zone is corrected for slab-dip angle.

of significant crustal contributions, either in the course of assimilating crust at high pressures (Hildreth & Moorbath, 1988) or as a result of mantle source contamination by forearc tectonic erosion (Stern, 1991; Kay *et al.*, 2005). The range of Sr-isotopic ratios decreases progressively to the south, and reaches an apparent minimum at ~37°S (Fig. 2a). The maximum in $^{143}Nd/^{144}Nd$ lies further to the south (Volcán Llaima; 38·6°S). Intermediate and silicic lavas from NLV have radiogenic isotopic compositions that fall within the regional variation trend and these values are indistinguishable from those at neighboring centers (Hildreth & Moorbath, 1988), whereas certain other geochemical parameters are unique to this center (Sellés *et al.*, 2004). The Holocene products of NLV, the main topic of this study, are the ones that most clearly show adakitic trace element characteristics, thereby distinguishing them from other evolved rocks of this arc (Fig. 2).

ANALYTICAL METHODS

Major elements were obtained by X-ray fluorescence (XRF) on fused glass discs on a Phillips PW 2400 spectrometer equipped with a rhodium tube at the University of Lausanne (Switzerland), following the methods described by Pfeifer *et al.* (1991). Most samples were also analyzed for trace elements by XRF on pressed-powder pellets. A subset of samples was analyzed by inductively coupled plasma–mass spectrometry (ICP-MS) at Harvard University. Standards MAR, BHVO-2, JB-2, BCR-2 and LUM37-3 were used for ICP-MS analyses. Sample dissolution was accomplished by acid attack in screw-top Teflon beakers. Trace element data obtained by ICP-MS are accurate to within ±5% on the basis of duplicate analyses. We have chosen to use Y, Sr, Rb, Ni, Cr, V, Zr, and Ba obtained by XRF and ICP-MS values of Sc, Cu, Ga, Nb, Cs, REE, Hf, Ta, Pb, Th, and U.

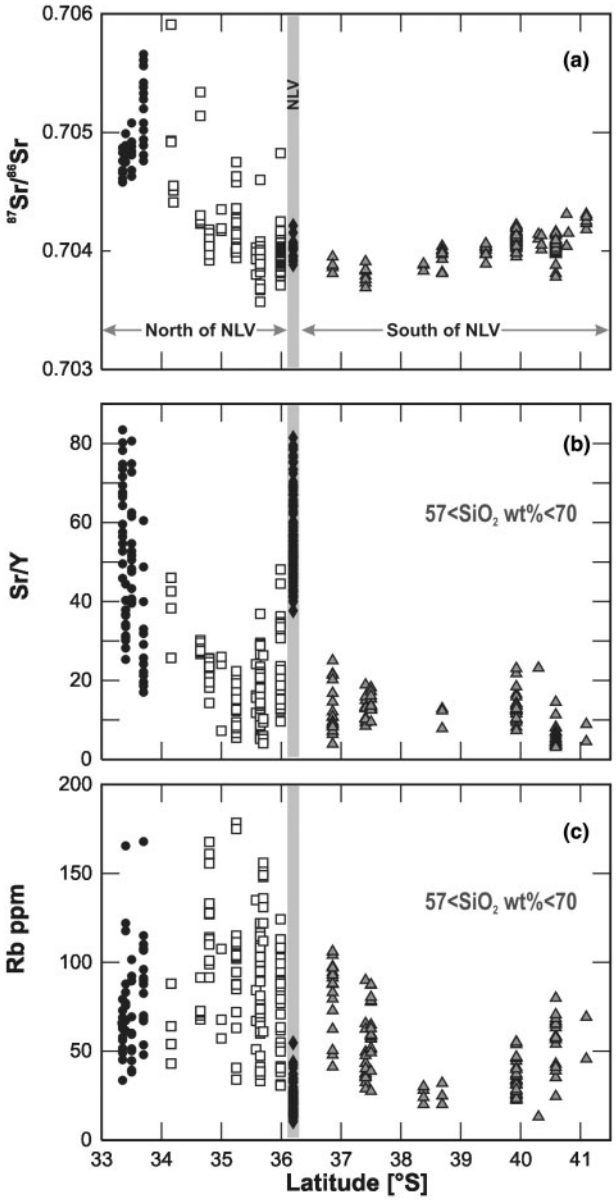

Fig. 2. Latitudinal variations of selected parameters in SVZ volcanic rocks; symbols as in Fig. 1. (a) Sr isotopic ratios; (b) Sr/Y; (c) Rb abundance. NLV samples are highlighted by a gray band. (b) and (c) have been filtered to show only samples with 57 <SiO_2 wt% <70. Data from Déruelle *et al.* (1983), Harmon *et al.* (1984), Hickey *et al.* (1986), Futa & Stern (1988), Gerlach *et al.* (1988), Hildreth & Moorbath (1988), Hickey-Vargas *et al.* (1989), McMillan *et al.* (1989), Tormey *et al.* (1991, 1995), López-Escobar *et al.* (1992), Tagiri *et al.* (1993), Déruelle & López-Escobar (1999), Dixon *et al.* (1999), Dungan *et al.* (2001), Sellés *et al.* (2004), Sruoga *et al.* (2005), Rodríguez (2006), and Sellés (2006).

The complete trace element dataset is available as an Electronic Appendix, available for downloading from http://www.petrology.oxfordjournals.org.

Isotope ratio measurements were performed by thermal ionization mass spectrometry (TIMS) at the University of Geneva using a seven-collector Finnigan MAT 262 system with extended geometry and stigmatic focusing using double Re filaments, on one of which a fraction of the purified Sr or Nd is loaded. The Sr isotopic ratios were corrected to an $^{88}Sr/^{86}Sr$ ratio of 8·375209 and normalized to the Eimer & Amend (E&A) $SrCO_3$ standard with $^{87}Sr/^{86}Sr = 0{\cdot}708000$ using an average of $0{\cdot}708056 \pm 5 \times 10^{-6}$ (2 SE), $n = 59$. Nd isotopic ratios were corrected for mass fractionation relative to a $^{146}Nd/^{144}Nd$ ratio of 0·7219 and normalized to the La Jolla standard value [$^{143}Nd/^{144}Nd = 0{\cdot}511835 \pm 4 \times 10^{-6}$ (2 SE), $n = 91$]. For each sample about 100 mg of rock powder was digested in 1 ml 14M HNO_3 + 4 ml 29M HF in a sealed Teflon beaker on a hot-plate at 140°C for 1 week. After drying, the residue was dissolved again in 3 ml 14M HNO_3 in a sealed Teflon beaker at 140°C for 24 h and then dried again on a hot-plate. The residue was dissolved in 2 ml of 1M HNO_3, centrifuged, and strontium and neodymium were separated by extraction chromatography using Eichrom's Sr, TRU and Ln resins in columns. The samples dissolved in HNO_3 were poured directly onto the Sr resin columns, where Sr was retained. The solutions collected at the bottom were passed through TRU resin columns, where the light rare earth elements (LREE) were selectively retained. The sample in the Sr resin columns was washed with 8M HNO_3 and then eluted with 0·05M HNO_3. The recovered Sr-enriched solution was dried and passed again through the same columns following the same steps as above to achieve an optimal purification of Sr. Nd purification was achieved by washing the TRU resin columns with 1M HNO_3 and then eluting LREE into Ln resin columns using 0·05M HNO_3. The samples in the Ln resin columns were subsequently washed with several milliliters of 0·2M HCl. The separation of Nd from Sm (essential to avoid isobaric interferences at masses 144, 148 and 150) was achieved by eluting Nd with 0·3M HCl and, if needed, Sm with 0·5M HCl.

Boron contents were determined at Rice University (Houston, TX, USA). Whole-rock powders were weighed and dissolved in HF and then dried at 70°C to prevent boron volatilization. Mannitol [$C_6H_8(OH)_6$; 10 µl] was added to help retain boron in solution. Solid precipitates were dissolved in HCl and then diluted in sub-boiled H_2O. The resulting solution was separated into three aliquots, two of which were spiked with known amounts of boron from a calibrated solution. The three aliquots were then analyzed by inductively coupled plasma atomic emission spectrometry (ICP-AES). Iron interference was corrected by using calibrated solutions containing B and Fe. One international rock standard and a blank were also analyzed following each group of three unknowns. The typical uncertainty for replicate analyses is ±4%.

Microprobe analyses were carried out using a five-spectrometer Cameca SX-50 at the University of Lausanne.

Operating conditions for all mineral analyses were as follows: accelerating voltage 15 kV, counting times 15–20 s on peak and 10 s on background, and focused beam diameter 1 μm. Volatile elements (Na, Cl, F) were always analyzed first. Beam current was 15 nA for plagioclase and amphibole and 20 nA for olivine, pyroxene, Fe–Ti oxides, and apatite. Standardization involved a set of natural and synthetic materials. Modal abundances were calculated by point counting 35 thin sections.

NEVADO DE LONGAVÍ VOLCANO (NLV) AND ITS HOLOCENE STRATIGRAPHY

NLV was constructed on gently folded Late Oligocene to Early Miocene continental volcaniclastic and sedimentary strata of the Cura-Mallín Formation, which are intruded by granitoid plutons of late Miocene age (Muñoz & Niemeyer, 1984). The eruptive products of NLV also overlap onto the northern remnants of Villalobos volcano, a large basaltic to basaltic andesitic Plio-Pleistocene edifice. NLV is composed primarily of thick andesitic flows that radiate from a central vent. Basalts and basaltic andesites predominate among basal units as old as 1 Ma, whereas dacitic compositions ($SiO_2 > 62$ wt%) are present exclusively in the Holocene products (Rodríguez, 2006; Sellés, 2006).

Holocene activity at NLV was concentrated in the summit area and within a pre-existing collapse bowl on the eastern flank of the edifice (Rodríguez, 2006). The Holocene sequence is dominated volumetrically by the early Río Blanco dacitic pumice fall deposit (~7·5 ka) and a younger near-summit dome extrusion that in large part collapsed to the east to form the Lomas Limpias block-and-ash flow deposits (~5·7 ka). The Río Blanco pyroclastic eruption produced a fallout deposit composed of crystal-rich (30 vol.%, vesicle free) dacitic pumices (~65–66 wt% SiO_2) that are up to 40 cm in diameter in proximal areas, and that extend from the summit area to the SE for ~20 km. The Lomas Limpias episode was characterized by the emplacement of a summit dacitic dome that partially collapsed to form a series of small-volume Merapi-type block-and-ash flow deposits. These unconsolidated, monolithologic, matrix-supported, and generally massive deposits were emplaced on the eastern flank of the volcano (~4 km^2). Variably vesiculated blocks of porphyritic dacite (~62–65 wt% SiO_2) contain quenched mafic magmatic enclaves (~2 vol.%).

Stratigraphically between the Río Blanco and the Lomas Limpias dacites is the Castillo Andesite (not dated), which is a hybrid magma that was generated by mixing of mafic and dacitic magmas similar in composition to the quenched mafic enclaves and the Holocene dacites, respectively. This lava will not be treated in as much detail as the dominantly dacitic Río Blanco and Lomas Limpias deposits; for further details the reader is referred to Rodríguez (2006).Amphibole-rich cumulate xenoliths up to 20 cm in diameter are present in some Holocene deposits and in some andesitic lavas from the main cone (Sellés, 2006). The mineral assemblages of these cumulates resemble those of the enclaves and dacites in that amphibole is always the main ferromagnesian phase.

PETROGRAPHY AND MINERAL CHEMISTRY OF THE HOLOCENE NLV

In the following sections we describe the petrography and mineral chemistry of the Holocene dacites and the mafic inclusions and cumulate xenoliths that they contain. In these descriptions we adopt the following convention: crystals larger than 2·5 mm are termed phenocrysts, microphenocrysts if they are between 2·5 and 0·1 mm, and microlites are below 0·1 mm.

Río Blanco and Lomas Limpias dacites

The Río Blanco phenocryst–microphenocryst mineral assemblage is dominated by plagioclase (~20 vol.%) and amphibole (~6 vol.%), with substantially less orthopyroxene (~2 vol.%), Fe–Ti oxides (~1 vol.%) and apatite (trace), in a glassy, highly vesicular groundmass (Fig. 3a and b). No large mafic enclaves have been observed but some pumices contain thin grey streaks. The porphyritic Lomas Limpias dacite contains the same mineral assemblage as Río Blanco pumices: plagioclase (~22 vol.%), amphibole (~8 vol.%), orthopyroxene (~2·5 vol.%), Fe–Ti oxides (~2·5 vol.%), plus accessory apatite and sulfides (trace) in a crystalline grey groundmass (Fig. 3c and d).

Plagioclase is the most abundant mineral phase in dacites. Most of the phenocrysts (up to 4 mm) and microphenocrysts in the Río Blanco pumices have compositions in the range of $An_{30–45}$ (Fig. 4a). Some are mantled by more calcic rims up to 100 μm thick ($An_{40–46}$, rarely up to An_{65}). Microlites are usually more calcic ($An_{40–68}$) than phenocryst cores. Plagioclase phenocrysts in Lomas Limpias dacite display a wide diversity of morphologies from equant to elongate, and some are grouped into synneusis aggregates (Vance, 1969). Partly resorbed plagioclase crystals, including completely sieved, sieve-cored, and sieve-ringed grains are common (Coombs *et al.*, 2000). Core compositions are in the range of $An_{30–55}$, but the dominant compositions are $An_{35–45}$ (Fig. 4b). Some crystals are rimmed by overgrowths (≤150 μm thick), usually precipitated on resorption surfaces, that are 10–20 mol% more An-rich than the cores of these crystals. Stubby to elongate microlites are normally zoned from $An_{65–45}$ cores to An_{30} rims, which is the same

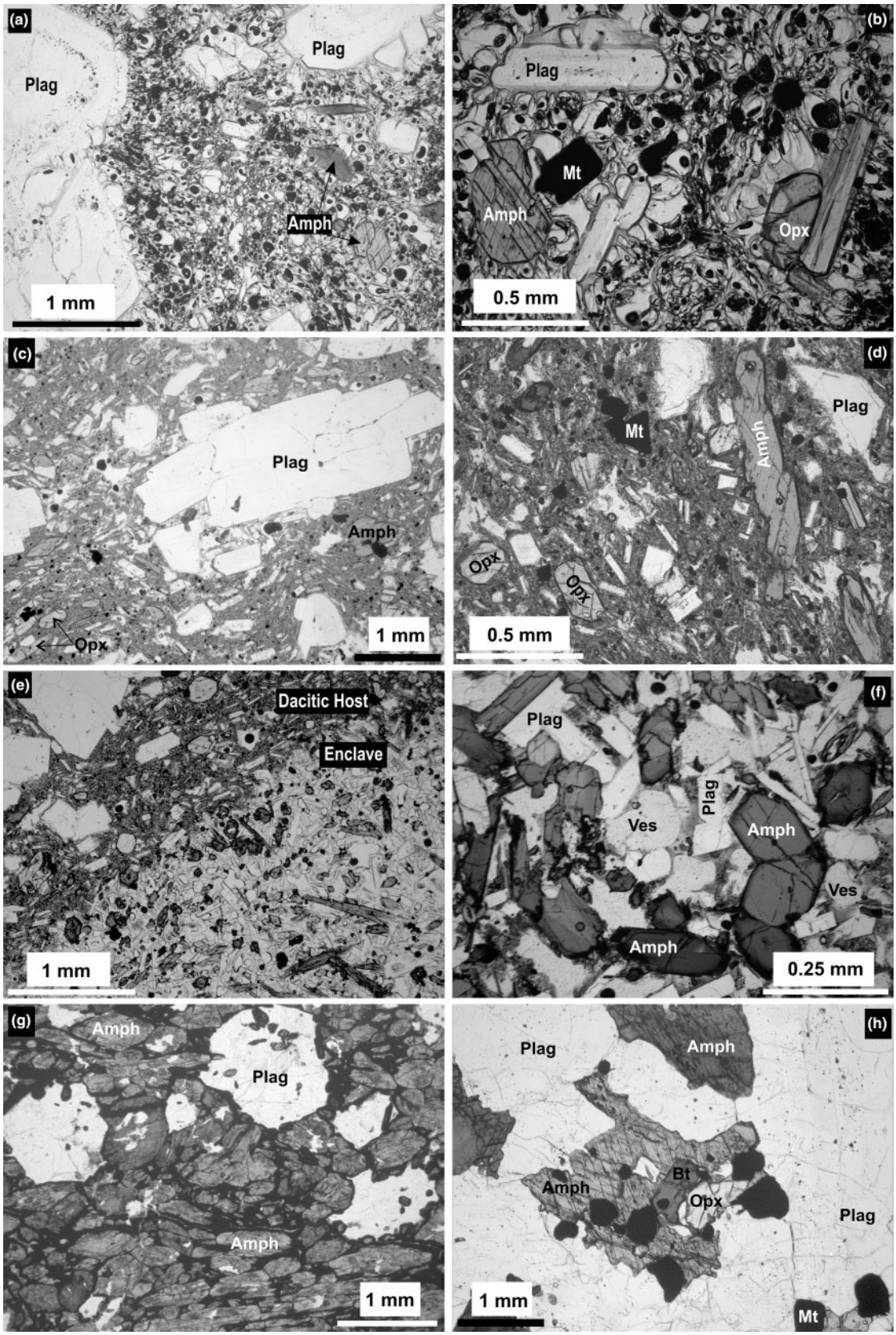
(a)
Plag
Plag
Amph
1 mm
(b)
Plag
Mt
Amph
Opx
0.5 mm
(c)
Plag
Amph
Opx
1 mm
(d)
Mt
Amph
Plag
Opx
Opx
0.5 mm
(e)
Dacitic Host
Enclave
1 mm
(f)
Plag
Plag
Ves
Amph
Ves
Amph
0.25 mm
(g)
Amph
Plag
Amph
1 mm
(h)
Plag
Amph
Bt
Amph
Opx
Plag
1 mm
Mt

range as for calcic overgrowths on partly resorbed phenocrysts.

Amphibole is the dominant ferromagnesian mineral in dacites (Fig. 3a to 3d). It forms euhedral to subhedral microphenocrysts (0·1–2·5 mm). Amphibole grains are usually homogeneous and rarely display disequilibrium textures, but in some samples a minority of amphibole grains are zoned and others have thin Fe-oxide rich reaction rims (<4 μm thick) related to oxidation and dehydrogenation during or after eruption (Garcia & Jacobson, 1979; Rutherford & Devine, 1988).

Two compositional groups of amphiboles have been defined in the Río Blanco and Lomas Limpias dacites on the basis of contrasting Al contents (Fig. 5a and b). High-Al amphiboles (10–13 wt% Al_2O_3; Table l; Supplementary Data) are mainly magnesiohastingsite, but a minor fraction of the analyses are tschermakite and pargasite (Leake *et al.*, 1997). The Mg-number [$Mg/(Mg + Fe^{total})$ in cation units] of high-Al amphiboles varies between 0·78 and 0·62 at a nearly constant Si/Al^{total} cation ratio of ~3 and A-site occupancy between 0·4 and 0·8. A second group of amphiboles with lower Al contents (5–10 wt% Al_2O_3) is the dominant amphibole type in the Río Blanco dacite, although rounded cores of high-Al amphibole mantled by low-Al rims are present. Low-Al amphibole constitutes approximately two-thirds of the total amount of amphibole crystals in the Lomas Limpias dacite. Low-Al amphiboles are magnesiohornblende with highly variable Si/Al^{total} (between 4 and 8), which positively correlates with Mg-number. Total alkali cations in the A-site are <~0·4. Cr_2O_3 contents are consistently low in low-Al amphiboles (mostly <0·1 wt%) whereas Cr_2O_3 is up to 1 wt% in high-Al amphiboles. Halogen contents are low (<0·09 wt% Cl, <0·24 wt% F) in both groups. Some high-Al amphiboles are continuously normally zoned toward low-Al compositions at the rims. Rare reversely zoned amphiboles with low-Al cores (6–9 wt% Al_2O_3) rimmed by high-Al amphibole (10–12 wt% Al_2O_3) are present near contacts between dacite and mafic enclaves.

Orthopyroxene occurs as euhedral to subhedral microphenocrysts in both dacites. Orthopyroxene in Lomas Limpias dacite (0·1–1 mm) is restricted in composition ($En_{66–69}Fs_{29–32}Wo_{0·7–2·4}$; Table 2; Supplementary Data), and similar compositions are present in Río Blanco pumices (Fig. 6). Exchange coefficients for the distribution of Mg and Fe between orthopyroxene and liquids ($K_D^{Fe/Mg}$) equivalent to bulk-rock dacite are in the range 0·42–0·44 in pumices and 0·40–0·42 in Lomas Limpias dacite. These are higher than experimentally determined values (Nakamura & Kushiro, 1970; Grove *et al.*, 1997, 2003), which suggests that opx crystallized from liquids more evolved than the whole-rock, in agreement with the observation that it is found only as isolated microphenocrysts and never as inclusions in other phases.

Fe–Ti oxides occur as homogeneous, euhedral to subhedral grains (<0·6 mm). Ilmenites with exsolution lamellae were avoided during microprobe analyses (see Supplementary Data). There is a compositional array of coexisting magnetites (14·3–20·6 mol% Usp) and ilmenites (55·5–66 mol% Ilm) in Río Blanco pumices. Ilmenites in the Lomas Limpias dacite have compositions nearly identical to those in the Río Blanco unit (55·5–66 mol% Ilm). Magnetite grains in Lomas Limpias dacite also overlap with Río Blanco dacite magnetites, but large crystals (up to 0·5 mm) are zoned from low-TiO_2 cores (15·5–19 mol% Usp; 5·2–6·5 wt% TiO_2) to high-Ti rims with up to 8–10 wt% TiO_2. Homogeneous, smaller magnetites (<0·35 mm) have high TiO_2 (7–9 wt%) in the range of the high-TiO_2 rims, and therefore probably represent late crystallization.

Quenched mafic enclaves

Quenched mafic enclaves of basaltic andesitic to andesitic composition (53·8–58·8 wt% SiO_2; anhydrous basis) constitute ~2 vol.% of the Lomas Limpias dacite, but are also found in lesser abundance in the Castillo Andesite. They range in size from 1 to 70 cm in diameter (usually <30 cm), and have ellipsoidal to spherical shapes, or, more rarely, angular or dyke-like forms. Contacts between host dacite and enclaves are sharp and some enclaves preserve chilled margins.

Magmatic enclaves contain plagioclase (~48 vol.%) and amphibole (~30 vol.%) along with minor orthopyroxene (~1·5 vol.%), Fe–Ti oxides (~3·5 vol.%) and olivine (<3 vol.%), in a vesicular matrix of pale brown microlite-free glass (~13 vol.%). Crystals are generally euhedral and have elongated to acicular morphologies (Fig. 3e and f). Acicular forms are characteristic of relatively fine-grained enclaves. Plagioclase and amphibole are interlocking and randomly oriented in dense diktytaxitic frameworks (Bacon, 1986).

Fig. 3. Representative textural relations. (a) Río Blanco pumice showing a large plagioclase (Plag) phenocryst with rounded resorption surfaces rich in melt inclusions, and amphibole (Amph) microphenocryst. (b) Detail of the vesicular texture of pumices, showing microphenocrysts of amphibole (Amph), orthopyroxene (Opx) and magnetite (Mt). The rounded morphology of amphibole may reflect rapid resorption by decompression. (c) Porphyritic texture of Lomas Limpias dacite, showing a large plagioclase phenocryst and microphenocrysts of amphibole, orthopyroxene, and Fe–Ti oxides. (d) Subhedral to euhedral crystals of amphibole, orthopyroxene, magnetite, and plagioclase in Lomas Limpias dacite. (e) Sharp contact between quenched mafic enclave and host dacite. (f) Detail of enclave texture characterized by randomly oriented plagioclase and amphibole microphenocrysts and rounded vesicles (Ves) in glass. (g) Amphibole gabbro cumulate with a strong subparallel alignment of amphibole crystals. (h) Amphibole diorite cumulate, showing subhedral plagioclase, amphibole, orthopyroxene, biotite (Bt) and magnetite.

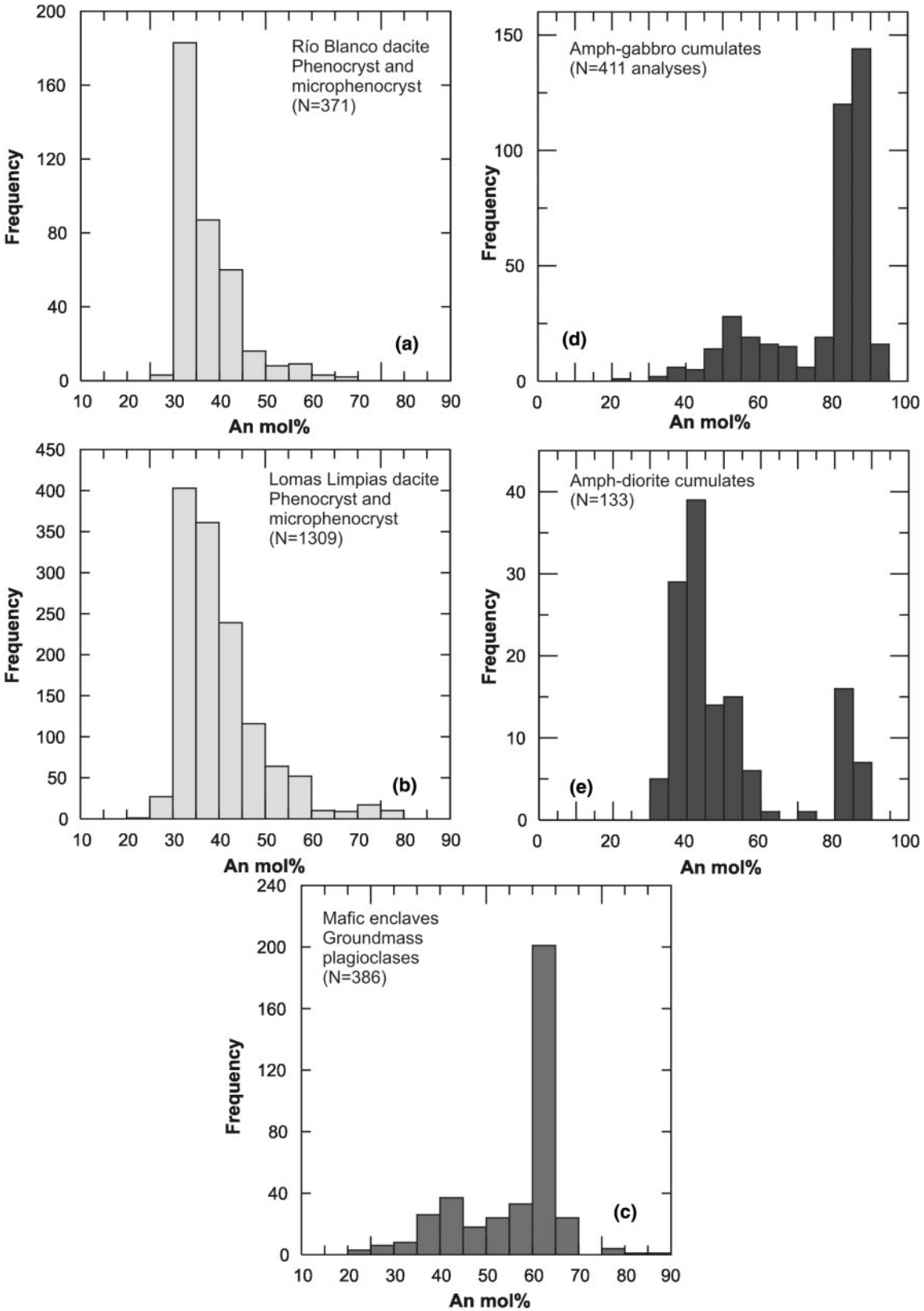

Fig. 4. Histograms of plagioclase composition (in terms of An mol%) for the different lithologies discussed in the text.

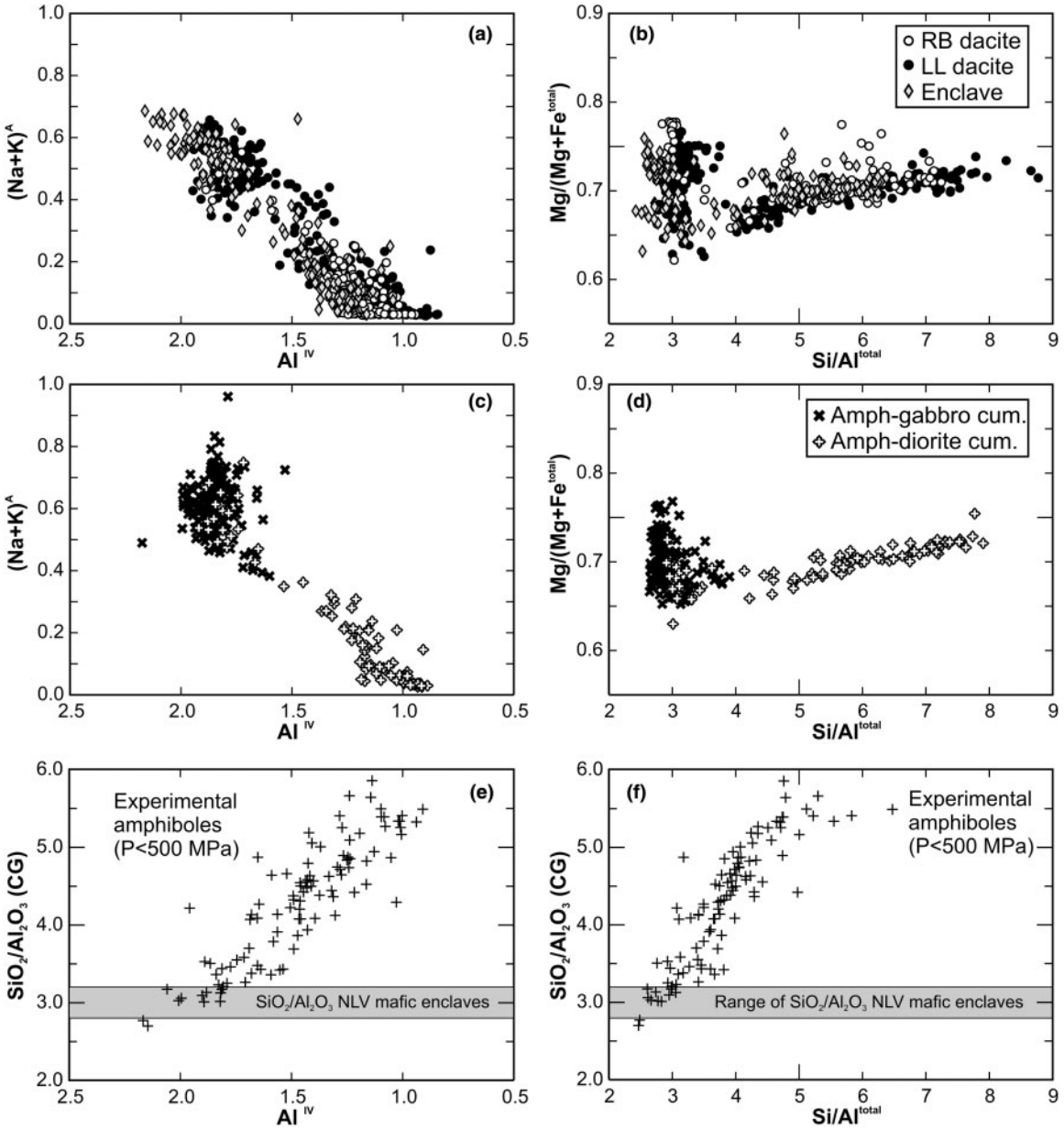

Fig. 5. Compositional variations of amphibole. (a, b) Río Blanco (RB) and Lomas Limpias (LL) dacites, and mafic enclaves; (c, d) amphibole-bearing gabbro and diorite cumulates; (e, f) experimental amphiboles plotted against the SiO_2/Al_2O_3 ratio of their coexisting glass (CG). Coexisting glass compositions span the range 52–78 wt% SiO_2. Data from Rutherford & Devine (1988), Sisson & Grove (1993), Grove *et al.* (1997, 2003), Moore & Carmichael (1998), Martel *et al.* (1999), Prouteau *et al.* (1999), Scaillet & Evans (1999), Hilyard *et al.* (2000), Costa *et al.* (2002), Pichavant *et al.* (2002), and Prouteau & Scaillet (2003). Structural formulae were calculated assuming 13 cations (excluding Ca, Na and K) and cations charge-balanced to 23 oxygens.

Plagioclase is the most abundant phase in enclaves. It occurs as acicular, elongated, prismatic, and tabular crystals (0·1–1 mm) that usually contain abundant primary melt inclusions. These are unzoned or normally zoned with dominant core compositions of $An_{70–60}$ and rim compositions near An_{40}, which in some cases can be as low as $An_{35–32}$ (Fig. 4c). Larger crystals of plagioclase (usually >0·8 mm) usually have resorbed cores and euhedral overgrowth rims with compositions similar to the rest of the plagioclase ($An_{60–40}$) in the enclaves. Plagioclase xenocrysts incorporated from the host dacite (<1%) occur in some enclaves. Such crystals are identified by larger sizes (1·2–2·8 mm) than generic enclave plagioclase, morphologies similar to plagioclase phenocrysts in host dacites, and by sieve-textured cores with rims of euhedral plagioclase that are normally zoned from

Table 1: Representative amphibole microprobe analyses

Host rock:	RB	RB	RB	RB	LL	LL	LL	LL	ME	ME
Sample:	7304	7304	7303	7303	7152	7152	7152	7152	7331	7331
Analysis:	Anf3-1	Anf3-4	Amp7-1	Amp7-4	A1-1	A1-4	A2-1	A2-3	A1-1	A1-2
wt%										
SiO_2	49·16	47·53	45·77	45·44	44·46	43·85	50·00	48·72	41·91	42·01
TiO_2	1·18	1·36	0·91	1·22	2·15	2·28	1·21	1·48	2·91	2·71
Al_2O_3	7·72	7·01	6·44	7·60	11·96	12·17	6·70	7·58	13·21	13·32
FeO*	12·41	11·55	12·20	12·43	10·60	9·87	11·25	11·89	9·80	10·32
MnO	0·36	0·28	0·32	0·29	0·13	0·11	0·33	0·27	0·13	0·08
MgO	16·02	15·26	16·66	16·00	15·55	15·47	16·39	15·67	15·16	14·98
CaO	10·59	10·44	10·51	10·56	11·34	11·65	10·83	11·04	11·45	11·63
Na_2O	1·53	1·40	1·27	1·62	2·62	2·62	1·45	1·68	2·81	2·71
K_2O	0·21	0·21	0·17	0·20	0·22	0·23	0·17	0·22	0·09	0·10
F	0·04	0·07	0·04	0·05	0·04	0·05	0·05	0·07	0·01	0·01
Cl	0·01	0·01	0·01	0·01	0·00	0·00	0·01	0·01	0·01	0·00
Cr_2O_3	0·04	0·00	0·02	0·00						
Total	99·25	95·12	94·34	95·40	99·13	98·38	98·51	98·76	97·49	97·89
Mg-no.	0·70	0·70	0·71	0·70	0·72	0·74	0·72	0·70	0·73	0·72

Host rock:	ME	ME	ADC	ADC	ADC	ADC	AGC	AGC	AGC	AGC
Sample:	7184	7184	NL033B	NL033B	NL033B	NL033B	NL120E	NL120E	NL120E	NL120E
Analysis:	Amp1-4	Amp3-1	anf2-1	anf2-9	anf4-14	anf4-1	anf3-8	anf2-2	anf1-12	anf2-6
wt%										
SiO_2	42·51	45·99	49·91	49·98	51·45	49·14	42·95	42·99	42·99	42·79
TiO_2	1·77	1·76	1·16	1·01	1·04	1·05	2·14	2·17	2·24	2·24
Al_2O_3	10·64	8·21	7·08	6·03	7·29	6·61	11·97	12·66	12·74	12·89
FeO*	13·12	10·37	12·23	11·83	11·20	12·03	11·55	11·84	11·91	11·54
MnO	0·33	0·30	0·34	0·39	0·34	0·33	0·19	0·20	0·19	0·19
MgO	14·09	16·70	16·17	16·44	14·62	15·96	14·44	14·36	14·49	14·38
CaO	10·96	10·93	10·87	11·08	10·20	10·99	11·28	11·54	11·47	11·59
Na_2O	2·10	1·68	1·60	1·29	1·37	1·42	2·86	3·33	2·90	2·95
K_2O	0·23	0·24	0·21	0·25	0·42	0·26	0·22	0·22	0·20	0·23
F	0·04	0·07	0·03	0·02	0·01	0·02	0·00	0·12	0·05	0·00
Cl	0·01	0·02	0·00	0·00	0·00	0·00	0·01	0·00	0·00	0·00
Cr_2O_3	0·00	0·07	0·02	0·04	0·02	0·00	0·05	0·09	0·04	0·04
Total	95·80	96·33	99·78	98·48	98·08	97·94	97·70	99·70	99·48	98·91
Mg-no.	0·66	0·74	0·70	0·71	0·70	0·70	0·69	0·68	0·68	0·69

*Total iron as FeO.
RB, Río Blanco dacite; LL, Lomas Limpias dacite; CA, Castillo Andesite; ME, mafic enclave; AGC, amphibole gabbro cumulate; ADC, amphibole diorite cumulate. Mg-number = $Mg/(Mg + Fe^{total})$.

$An_{61–69}$ to $An_{51–34}$. The compositions of these rims overlap with those of the enclave groundmass plagioclase.

Amphibole is the principal ferromagnesian phase in enclaves. It forms acicular to euhedral elongated crystals ranging from 0·1 to 1·4 mm in length. Most of the amphiboles in enclaves have high-Al compositions (10–13·6 wt% Al_2O_3; Table 1; Supplementary Data) and are classified as magnesiohastingsite or tschermakite (Leake *et al.*, 1997). Low-Al amphiboles (8–6·7 wt% Al_2O_3) are less abundant and usually form smaller crystals than those with high-Al compositions (Fig. 5a and b). Low-Al amphibole is also present as thin rims on some normally zoned amphiboles containing high-Al cores. Sparse xenocrystic low-Al amphiboles, transferred from the host dacite into enclaves,

Table 2: Representative olivine (ol), orthopyroxene (opx), and clinopyroxene (cpx) microprobe analyses

Host rock:	ME	ME	ME	ME	ME	ME	RB	RB	RB
Sample:	7331	7331	7331	7154	7154	7154	7304	7304	7304
Analysis:	OL1-L1__7	OL7-L1__9	OL8-2	EOpx1	EOpx2	EOpxb12	PX1	PX2	PX4
Mineral:	Ol	Ol	Ol	Opx	Opx	Opx	Opx	Opx	Opx
wt%									
SiO_2	39·48	39·32	39·13	52·98	53·03	52·93	52·50	52·78	53·09
TiO_2	0·06	0·02	0·00	0·20	0·21	0·11	0·09	0·08	0·10
Al_2O_3	0·03	0·03	0·01	2·09	1·90	0·71	0·89	0·57	0·93
FeO*	19·18	17·94	18·43	17·78	17·72	19·83	19·47	19·49	19·51
MnO	0·27	0·23	0·29	0·97	0·94	0·82	0·82	0·84	0·82
MgO	40·78	42·07	41·88	25·10	25·35	24·97	24·83	25·03	25·26
CaO	0·11	0·14	0·14	0·42	0·43	0·48	0·43	0·43	0·42
Na_2O	0·00	0·00	0·00	0·02	0·02	0·01	0·03	0·01	0·01
Cr_2O_3	0·01	0·00	0·02	0·00	0·00	0·00	0·00	0·00	0·00
NiO	0·13	0·16	0·16	0·00	0·00	0·02	0·00	0·00	0·00
Total	100·05	99·91	100·07	99·57	99·59	99·89	99·07	99·24	100·15
Mg-no.	0·79	0·81	0·80	0·72	0·72	0·69	0·69	0·70	0·70

Host rock:	LL	LL	LL	LL	ADC	ADC	AGC	AGC	AGC
Sample:	7152	7152	7152	7152	NL033B	NL033B	NL129C	NL129C	NL129C
Analysis:	Opx1	Opx2	Opx10	Opx13	px4-L1__9	px4-L1__10	px4-L1__9	px3-8-incl	px1-8-incl
Mineral:	Opx	Opx	Opx	Opx	Opx	Opx	Opx	Opx	Cpx
wt%									
SiO_2	53·36	53·66	53·60	53·38	53·26	53·38	53·26	54·52	51·85
TiO_2	0·12	0·10	0·11	0·11	0·13	0·10	0·13	0·15	0·38
Al_2O_3	1·02	0·77	0·76	0·69	1·02	0·90	1·02	2·01	3·17
FeO*	19·16	19·31	19·77	19·50	19·52	19·18	19·52	13·68	6·71
MnO	0·86	0·88	0·87	0·82	0·88	0·83	0·88	0·38	0·21
MgO	24·37	24·53	23·95	24·15	25·04	25·00	25·04	28·59	15·41
CaO	0·51	0·44	0·50	0·62	0·51	0·55	0·51	0·69	21·82
Na_2O					0·03	0·04	0·03	0·00	0·00
Cr_2O_3	0·01	0·01	0·01	0·00	0·01	0·00	0·01	0·03	0·04
NiO	0·00	0·00	0·00	0·00	0·00	0·00	0·00	0·03	0·03
Total	99·42	99·69	99·56	99·27	100·41	99·97	100·41	100·07	99·61
Mg-no.	0·69	0·69	0·68	0·69	0·70	0·70	0·70	0·79	0·80

*Total iron as FeO.
RB, Río Blanco dacite; LL, Lomas Limpias dacite; ME, mafic enclave; AGC, amphibole gabbro cumulate; ADC, amphibole diorite cumulate. Mg-number = $Mg/(Mg + Fe^{total})$.

are rimmed by high-Al amphibole. High-Al amphiboles are close in composition to amphiboles produced experimentally in equilibrium with andesitic and basaltic andesitic liquids (i.e. coexisting liquids with $SiO_2/Al_2O_3 <\sim 3{\cdot}2$; see Fig. 5e and f; references in figure caption).

Orthopyroxene occurs in enclaves in low proportions as euhedral, elongated, nearly homogeneous microphenocrysts (0·1–0·8 mm) with compositions slightly more mafic than orthopyroxenes in the dacites ($En_{67–72}Fs_{27–32}Wo_{0·6–1·5}$; Fig. 6 and Table 2; Supplementary Data). The K_D for the distribution of Mg and Fe between orthopyroxene and liquid compositions equivalent to the bulk rock (0·39–0·42) is higher than published equilibrium values (Nakamura & Kushiro, 1970; Grove *et al.*, 1997, 2003). This is consistent with late crystallization of orthopyroxene, as is observed for opx in dacites.

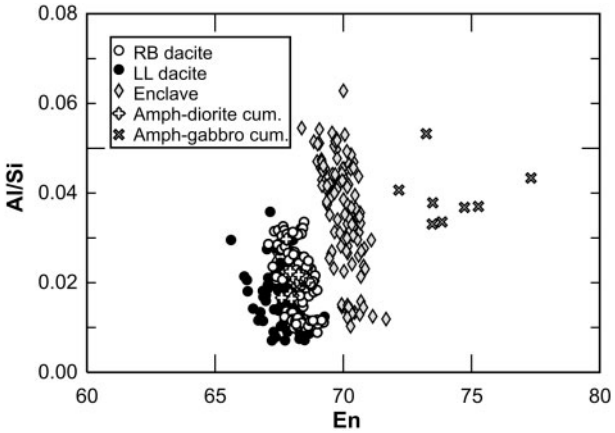

Fig. 6. Al/Si (cations) vs mole% enstatite (En) showing the compositional variation of orthopyroxenes from Río Blanco (RB) and Lomas Limpias (LL) dacites, enclaves, and amphibole-bearing cumulates. It should be noted that the orthopyroxene compositions in diorites are indistinguishable from those in dacites.

Olivine occurs in the least evolved enclaves as euhedral to subhedral (0·2–2 mm) homogeneous grains with compositions in the restricted range of $Fo_{78–80}$ (Table 2). They usually contain small (<0·05 mm) Cr-spinel inclusions with 10–17·5 wt% Cr_2O_3, 15–26 wt% Al_2O_3, and 3·5–9·2 wt% MgO. Exchange coefficients for the distribution of Mg and Fe between olivine and host liquids with compositions similar to the enclaves are around 0·28–0·30, which are in agreement with experimentally obtained values (Roeder & Emslie, 1970; Ulmer, 1989; Grove *et al.*, 2003). These olivine compositions are consistent with near-liquidus crystallization from host basaltic andesitic magmas.

Fe–Ti oxides form euhedral to subhedral grains (0·08–0·4 mm) in enclaves. Only magnetite (7·5–12 wt% TiO_2; 79–84 wt% FeO^{total}) is present in the least evolved enclaves, whereas less pristine enclaves contain homogeneous magnetite (15–16 mol% Usp and 5·0–7·2 wt% TiO_2), and minor ilmenite (60–63 mol% Ilm).

Amphibole-bearing cumulates

Amphibole-bearing cumulate xenoliths present in young NLV lavas are of two main types, amphibole gabbros and biotite-bearing amphibole diorites. Amphibole gabbros consist almost entirely of coarse (1–10 mm) amphibole and plagioclase crystals in variable proportions, wherein the most amphibole-rich varieties consist of up to 90 vol.% of this phase. Minor pyroxene and olivine are sparsely present as small, rounded relics within amphibole cores. Iron oxides and apatite are present in low abundances, and Cu-sulfides and pyrrhotite occur in trace amounts. Polygonal interstices are occupied by a microlite-rich glass or a fine-grained groundmass that usually constitutes 3–8 vol.% of the rock (up to 30–45% in a few cases). The most amphibole-rich samples are characterized by planar mineral orientations and subordinate interstitial plagioclase suggestive of post-cumulus compaction (Fig. 3g). Glass-rich samples are characterized by a loosely packed network of euhedral plagioclase and amphibole crystals and large polygonal pockets of vesicular dacitic glass with minute plagioclase and oxide microlites, suggesting that they were only partly solid when they were incorporated into the host lava. Amphibole diorites have a more evolved mineralogy relative to the gabbros (Fig. 3h). They contain abundant plagioclase (~60 vol.%) and amphibole (~30 vol.%) and minor amounts of Fe–Ti-oxides, orthopyroxene, biotite, quartz, and interstitial vesicular glass.

Plagioclase compositions in gabbros are characterized by weakly zoned calcic cores ($An_{80–92}$) with albite-rich rims (down to An_{30}). The widths of these rims range from a few microns in some samples to hundreds of microns in others. Textural relationships suggest that calcic plagioclase crystallized simultaneously with or shortly after amphibole, and that the sodic rims are post-cumulus (Sellés, 2006). Plagioclase in the dioritic cumulates is generally more sodic ($An_{50–35}$), although some calcic cores ($An_{80–90}$) are present (Fig. 4d and e).

Amphibole gabbro cumulates are characterized by magnesiohastingsites with high-Al contents (14–10 wt% Al_2O_3; Table 1; Supplementary Data) and up to 1 wt% Cr_2O_3. These overlap in composition with the high-Al amphiboles from the dacites and the mafic enclaves (Fig. 5c and d). Amphiboles in the diorites have a wide range of compositions between 5 and 12 wt% Al_2O_3, but low-Al amphibole (magnesiohornblende) predominates over high-Al compositions. High-Al amphibole cores in the diorites overlap with magnesiohastingsite compositions present in amphibole gabbros, mafic enclaves, and dacites, whereas low-Al amphiboles are similar to the low-Al amphiboles in enclaves and dacites (Fig. 5c and d).

Olivine and pyroxene are present in gabbros exclusively as inclusions in high-Al amphiboles. Olivine is mostly $Fo_{\sim 80}$, and is similar to phenocrysts in mafic enclaves, but a few analyses record higher Fo contents ($\leq Fo_{93}$). Orthopyroxene inclusions in gabbros are significantly more mafic ($En_{72–83}Fs_{15–26}Wo_{1·3–2}$) than the late-crystallized grains in dacites and mafic enclaves. Orthopyroxene in diorites, on the other hand, appears as a late phase, often together with biotite and quartz, and its restricted composition ($En_{67·6–68·6}Fs_{30·4–31·4}Wo_{0·9–1}$) overlaps the range of orthopyroxenes in the dacites (Fig. 6). Clinopyroxene inclusions ($En_{42–45}Fs_{9–11}Wo_{44–47}$) in amphibole gabbros are rare.

WHOLE-ROCK CHEMISTRY

The Holocene NLV dacites (61·6–65·8 wt% SiO_2; anhydrous basis; Fig. 7) are the most evolved products of this volcano (Table 3; Supplementary Data).

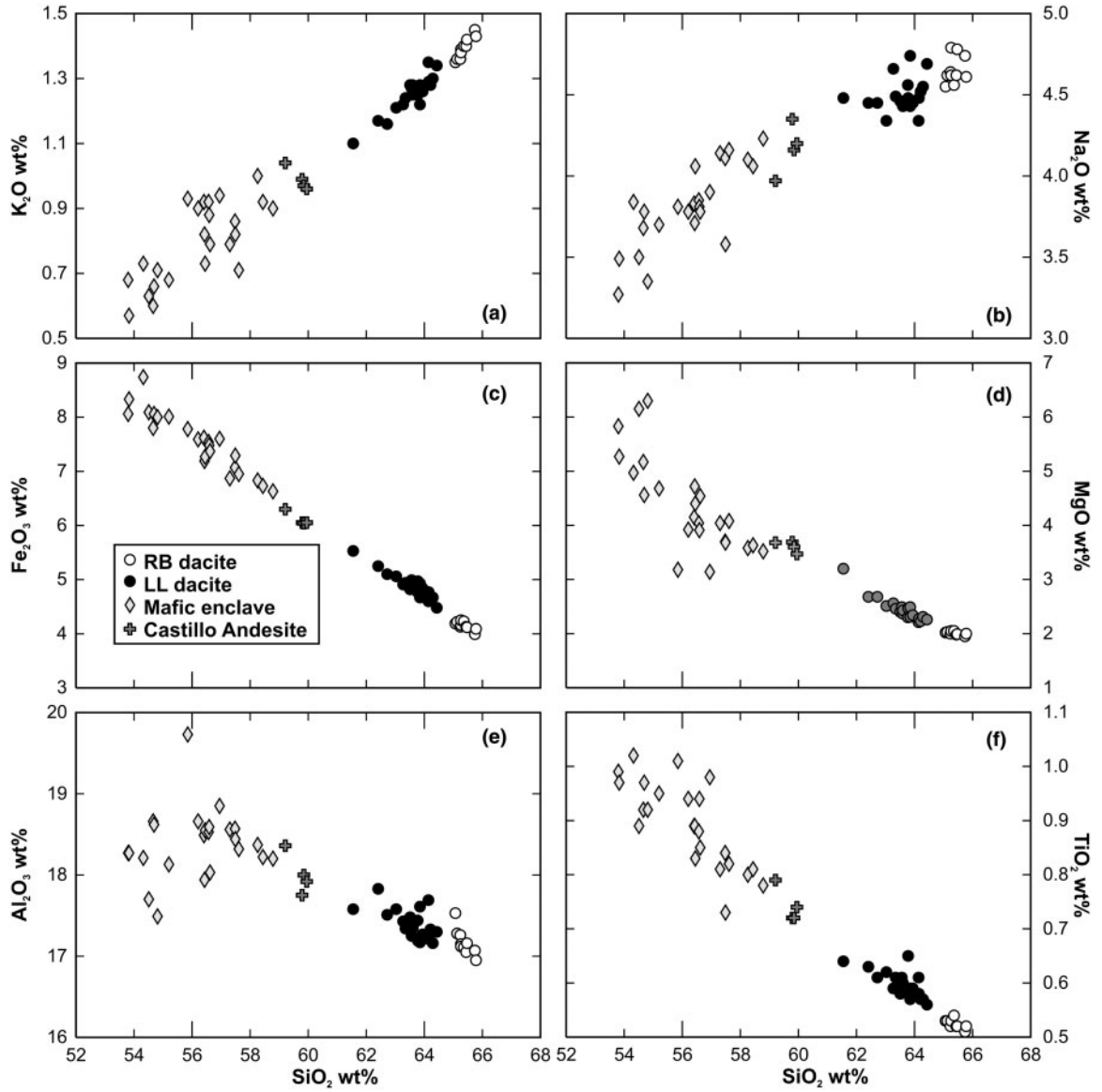

Fig. 7. Whole-rock major element chemical variation of Holocene NLV lavas and enclaves. Major elements normalized to 100% anhydrous basis. (See text and Table 3 for details.)

Table 3: Representative whole-rock analyses for major and trace elements

Sample:	8704	7154	7331	7134	LCBS01.1	NL015A	8711	7152	7304	9392	NL120E	NL033B
Rock:	ME	ME	ME	ME	CA	CA	LL	LL	RB	RB	AGC	ADC
wt%												
SiO_2	53·80	53·83	54·32	58·44	59·79	59·95	63·78	64·15	65·13	65·26	43·77	50·26
TiO_2	0·99	0·97	1·02	0·81	0·72	0·74	0·65	0·58	0·53	0·53	1·78	0·99
Al_2O_3	18·27	18·27	18·21	18·22	17·75	17·92	17·19	17·21	17·28	17·12	16·28	19·94
Fe_2O_3	8·06	8·33	8·74	6·73	6·05	6·05	4·97	4·77	4·22	4·25	11·74	9·46
MnO	0·12	0·13	0·13	0·11	0·10	0·10	0·09	0·09	0·08	0·08	0·22	0·15

(continued)

Table 3: Continued

Sample:	8704	7154	7331	7134	LCBS01.1	NL015A	8711	7152	7304	9392	NL120E	NL033B
Rock:	ME	ME	ME	ME	CA	CA	LL	LL	RB	RB	AGC	ADC
MgO	5·83	5·27	4·97	3·63	3·69	3·47	2·47	2·27	2·03	2·05	12·27	5·39
CaO	8·85	8·99	7·79	6·85	6·37	6·41	4·92	4·97	4·58	4·54	11·60	9·60
Na_2O	3·27	3·49	3·84	4·06	4·35	4·20	4·48	4·48	4·62	4·62	2·13	3·75
K_2O	0·68	0·57	0·73	0·92	0·99	0·96	1·26	1·29	1·36	1·38	0·17	0·24
P_2O_5	0·12	0·16	0·24	0·20	0·19	0·20	0·19	0·18	0·17	0·17	0·04	0·20
LOI	0·28	0·35	0·08	0·27	−0·15	0·31	−0·10	0·10	0·79	1·17	1·39	0·11
Total	100·01	99·47	99·12	99·66	99·28	98·81	100·59	99·94	100·03	100·27	99·03	99·65
ppm												
Zr*	83	86	103	117	104	106	122	127	124	125	22	
Y*	14·9	17·1	13	11	9·8	9·4	7·9	8	7·2	7·2	18·4	
Sr*	524	627	677	657	629	644	596	587	573	566	420	
Rb*	10·1	7·1	9·2	16	15·4	15·3	23·9	23·6	25·9	26·4	2·6	
Ni*	46	31	34	32	45	43	17	19	16	16	295	
Cr*	87	85	71	37	77	62	47	24	24	31	569	
V*	206	209	169	130	117	109	73	76	57	52	346	
Ba*	236	217	248	352	353	320	431	438	486	509	123	
B†	23·5	19·3	17·4	33·2	21·4	36·2	36·9	44·0	49·0	49·0	4·3	
Sc	30·5	30·2	16·9	13·5	13·1	12·5	10·1	7·2	7·8	6·7	79·8	18·8
Cu	83·3	173·0	46·1	104·1	34·1	63·6	22·9	21·6	22·9	35·6	46·5	188·1
Ga		18·9	20·4			20·1	20·0	19·6	19·3	19·0	17·5	22·7
Nb	2·4	2·6	3·1	3·5	3·2	3·1	4·0	3·9	3·8	3·6	1·4	2·7
Cs	0·97	0·75	0·81	1·35	0·73	1·41	1·73	1·93	2·16	2·14	1·65	0·20
La	7·9	9·2	9·8	11·2	10·9	10·6	13·3	11·6	12·2	12·5	2·7	8·4
Ce	18·8	23·6	23·0	24·2	23·7	23·1	28·0	24·0	25·4	26·1	10·0	22·1
Pr	2·57	3·44	3·12	3·26	2·97	3·05	3·08	3·26	3·04	3·09	2·06	3·29
Nd	11·8	15·1	14·6	13·7	12·6	12·7	12·3	13·2	12·3	13·0	12·3	15·3
Sm	2·95	3·49	3·32	2·85	2·74	2·57	2·35	2·49	2·25	2·19	3·95	3·41
Eu	1·04	1·29	1·14	0·96	0·89	0·87	0·85	0·84	0·77	0·77	1·35	1·22
Gd	3·04	3·27	3·22	2·79	2·57	2·34	2·12	2·14	1·95	2·02	4·15	3·23
Tb	0·46	0·52	0·45	0·38	0·34	0·35	0·32	0·30	0·29	0·30	0·65	0·45
Dy	2·72	2·98	2·49	2·13	1·81	1·83	1·46	1·57	1·31	1·35	3·81	2·46
Ho	0·56	0·63	0·47	0·40	0·35	0·35	0·29	0·30	0·27	0·25	0·74	0·47
Er	1·50	1·75	1·25	1·07	0·91	0·90	0·75	0·78	0·65	0·67	1·98	1·25
Yb	1·40	1·65	1·11	0·95	0·83	0·81	0·68	0·75	0·62	0·63	1·61	1·23
Lu	0·21	0·25	0·17	0·15	0·12	0·13	0·10	0·11	0·09	0·10	0·23	0·17
Hf	1·89	1·73	2·41	2·27	1·85	2·24	2·28	2·46	2·17	2·18	1·26	0·87
Ta	0·14					0·21	0·25		0·24	0·25	0·07	0·14
Pb	6·3	7·2	8·3	8·0	7·6	10·1	13·3	10·7	13·8	13·5	1·0	5·9
Th	0·92	1·06	0·80	1·19	1·15	1·28	2·13	1·44	2·21	2·14	0·07	0·64
U	0·26	0·31	0·23	0·34	0·30	0·32	0·52	0·50	0·55	0·55	0·01	

Major elements are normalized to 100%, all Fe as Fe_2O_3; analytical loss on ignition (LOI) and total are reported. ME, mafic enclave; CA, Castillo Andesite; LL, Lomas Limpias dacite; RB, Río Blanco dacite; AGC, amphibole gabbro cumulate; ADC, amphibole diorite cumulate. (See Electronic Appendix for the complete set of analyses.) Trace elements were determined by ICP-MS except as indicated.
*Trace elements determined by XRF.
†Trace elements determined by ICP-AES.

They are characterized by high concentrations of Al_2O_3 (17–17·8 wt%), CaO (4·4–5·7 wt%), MgO (2–3·2 wt%), and Sr (540–600 ppm) relative to other SVZ volcanoes (Sellés *et al.*, 2004), in combination with significantly lower concentrations of incompatible elements such as K, Rb, Ba, Th, Nb, Zr, Hf, Ce, Y, and REE (Fig. 8a). In particular, middle REE (MREE) and heavy REE (HREE) in NLV dacites are very low (e.g. Yb 0·61–0·86 ppm, ~2·6–4 times the chondritic value) compared with similarly evolved SVZ rocks, and the La/Yb and Sr/Y ratios are comparable with those of lavas erupted through the northern part of the arc where the crust is thickest and garnet is inferred to be a residual phase (Hildreth & Moorbath, 1988; Fig. 8a).

Quenched mafic enclaves (53·8–58·8 wt% SiO_2; Fig. 7) in Lomas Limpias dacite, the most mafic Holocene NLV magmas, have major element compositions similar to those of other SVZ magmas of the same silica content (e.g. Hickey *et al.*, 1986; Gerlach *et al.*, 1988; López-Escobar *et al.*, 1995a; Tormey *et al.*, 1995). They define variably scattered but well-defined compositional trends of increasing Al_2O_3, K_2O, and Na_2O with increasing silica. Even the most mafic NLV enclaves have low contents of MgO (<6·5 wt%; Table 3), V, Cr (<250 ppm), and Ni (<80 ppm) which indicate that they have undergone significant fractionation from more primitive melts. NLV enclaves are also low in the most incompatible trace elements when compared with similar basaltic andesitic compositions from other SVZ centers. Concentrations of K_2O (<0·7 wt%), Rb (~10 ppm), Zr (~90 ppm), Hf (~1·8 ppm), Th (~0·8 ppm), and U (~0·2 ppm) in the least evolved enclaves are lower than or close to those of lavas with similar silica contents at Villarrica, Llaima, and Calbuco volcanoes, which have the lowest previously reported concentrations of such elements in the SVZ (Hickey *et al.*, 1986; Hickey-Vargas *et al.*, 1989; López-Escobar *et al.*, 1995b). Boron concentrations in enclaves (17–33 ppm), on the contrary, are among the highest measured values for SVZ lavas of this composition (W. Leeman, unpublished data). Ratios of B to immobile trace elements (e.g. B/Th, B/Zr, B/Nb) are relatively constant from mafic enclaves to dacites, and are significantly higher than in any other SVZ volcano (Fig. 9e). Similarly, ratios of other fluid-mobile (Ba, Pb, Sr) to fluid-immobile (Zr, Nb, Th) elements are higher in the Holocene NLV than in the rest of the SVZ (Fig. 9e).

Amphibole-bearing cumulates cover a range of whole-rock compositions from nearly basaltic to the average composition of high-Al amphibole, and this trend reflects increasing modal abundances of this phase. Amphibole gabbro cumulates have lower abundances of many incompatible element than do NLV basalts (Sellés *et al.*, 2004; Sellés, 2006), but are relatively enriched in elements such as Ti, MREE, and HREE, for which amphibole has some affinity (e.g. Dalpé & Baker, 2000). MgO, TiO_2, Cr, and Ni are high in samples with high modal amphibole. The compositions of interstitial glasses from two glass-rich samples are dacitic (62 and 66 wt% SiO_2; Sellés, 2006) and they share the characteristic features of the dacites, such as high Al_2O_3 (19·22 and 17·12 wt%) and low K_2O (1·43 and 0·97 wt%), low Rb (20·3 and 12 ppm), low Ba (342 and 341 ppm), and low Y (10·4 and 4·6 ppm). Amphibole diorite cumulates have whole-rock compositions that overlap with the compositions of NLV basalts (Sellés, 2006), except for lower K_2O (<0·28 wt%), Rb (<2·7 ppm), Zr (<52 ppm), and Hf (<0·9 ppm) in the cumulates.

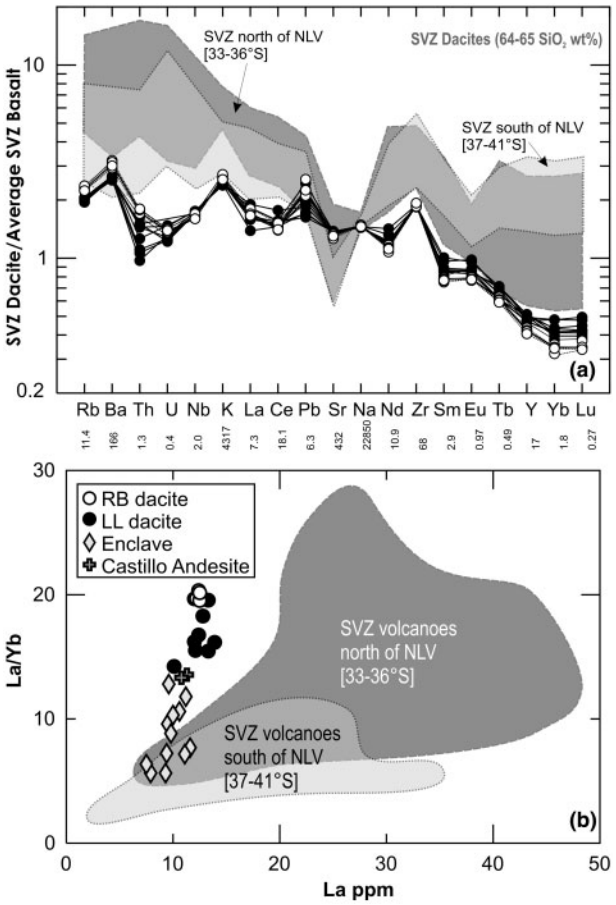

Fig. 8. (a) Multi-element comparison of NLV dacites with dacites of similar SiO_2 content from other centers of the SVZ (RB, Río Blanco dacite; LL, Lomas Limpias dacite). Data are normalized to an average of 32 basalts from the SVZ (normalization values in ppm given below the diagram) to highlight the differences between dacites. Data used to define the SVZ fields are from sources cited in Fig. 2 and Ferguson *et al.* (1992), López-Escobar *et al.* (1995*a*) and Costa & Singer (2002). (b) Comparison of NLV magmas with those of the SVZ in terms of La vs La/Yb. The divergence of the subvertical trend toward high La/Yb at nearly constant La concentration defined by the NLV data requires a distinct origin.

Isotopic compositions

The Sr and Nd isotopic compositions of dacites, enclaves, and one amphibole gabbro cumulate are in the range

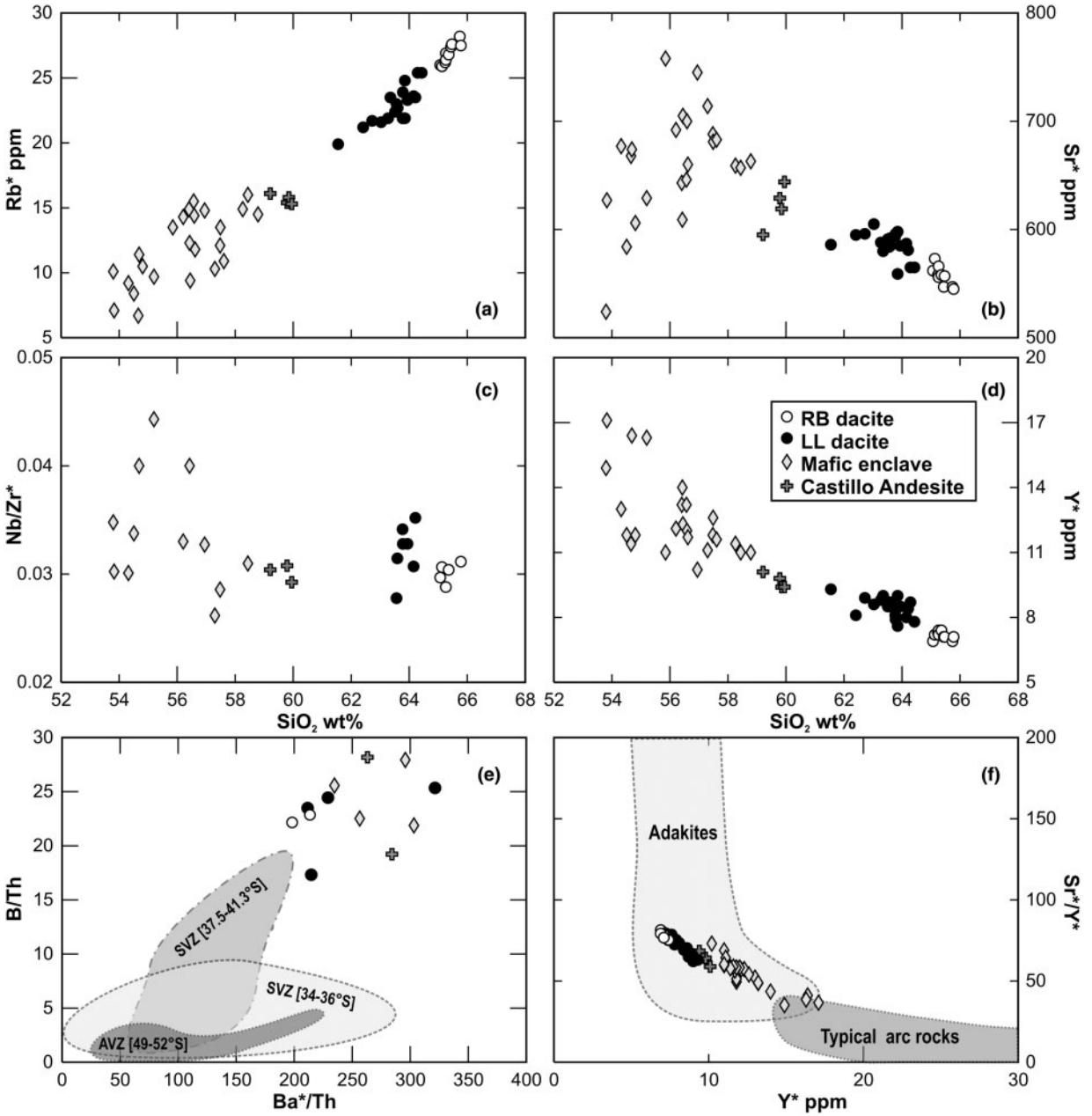

Fig. 9. Selected trace element concentrations and ratios for Holocene NLV magmas. In this and subsequent diagrams, elements marked with asterisk (*) refer to XRF analyses. (a) Rb^* vs silica; (b) Sr^* (ppm) vs wt% SiO_2; (c) Nb/Zr^* vs SiO_2; (d) Y^* vs SiO_2; (e) B/Th vs Ba^*/Th ratios, for which Holocene NLV lavas exhibit the highest values in the region (W. Leeman, unpublished data). It should be noted that adakites from a nominally hot-slab subduction environment (AVZ, Stern & Kilian, 1996) differ substantially from SVZ lavas for these parameters. (f) Sr^*/Y^* vs Y^*.

$^{143}Nd/^{144}Nd = 0{\cdot}512770–0{\cdot}512812$ and $^{87}Sr/^{86}Sr = 0{\cdot}70392–0{\cdot}70407$ (Table 4). These ranges are similar to those of main-cone NLV andesites (Hildreth & Moorbath, 1988; Sellés, 2006) as well as those of lavas from volcanoes located south of NLV (36·5–40°S), which generally do not manifest the effects of significant upper crustal assimilation (Hickey *et al.*, 1984, 1986; Gerlach *et al.*, 1988; Hildreth & Moorbath, 1988; Hickey-Vargas *et al.*, 1989; López-Escobar *et al.*, 1995a) (Fig. 10). The role of crustal assimilation at NLV is difficult to assess in this part of the SVZ entirely on the basis of isotopic variations, because of the apparently low isotopic contrast between Quaternary magmas and Miocene granitoid plutons on which the arc is largely constructed (Davidson *et al.*, 1987; Nelson *et al.*, 1999; Lucassen *et al.*, 2004; R. Spikings, unpublished data). The low abundances of most incompatible elements in

Table 4: Sr and Nd isotopic composition of NLV samples discussed in text

Sample code	Sample type	$^{143}Nd/^{144}Nd$	±2σ	$^{87}Sr/^{86}Sr$	±2σ
7304	RB	0·512801	0·000005	0·70402	0·00001
7152	LL	0·512784	0·000003	0·70402	0·00001
7204	LL	0·512799	0·000004	0·70401	0·00001
8715	LL	0·512780	0·000005	0·70404	0·00001
7331	ME	0·512805	0·000005	0·70392	0·00001
7154	ME	0·512777	0·000005	0·70403	0·00001
7134	ME	0·512793	0·000010	0·70404	0·00001
8704	ME	0·512812	0·000003	0·70407	0·00001
NL015A	CA	0·512797	0·000003	0·70402	0·00001
LCBS01.1	CA	0·512766	0·000004	0·70401	0·00001
NL120E	AGC	0·512770	0·000004	0·70398	0·00001

RB, Río Blanco dacite; LL, Lomas Limpias dacite; CA, Castillo Andesite; ME, mafic enclave; AGC, amphibole gabbro cumulate.

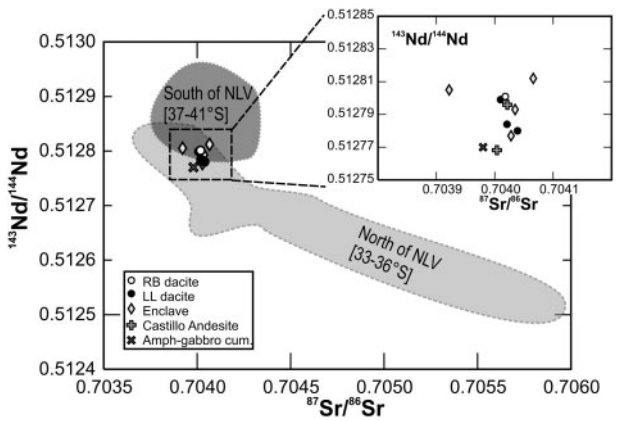

Fig. 10. Sr vs Nd isotopic ratios for Río Blanco (RB) and Lomas Limpias (LL) dacites, Castillo Andesite, mafic enclaves, and one amphibole gabbro cumulate. Fields defined for SVZ volcanoes to the north and south of NLV are shown for comparison. Data sources as in Figs 2 and 3.

NLV dacites (Fig. 8) place stringent limits on the amount of upper crustal participation in their petrogenesis.

DISCUSSION

Pre-eruptive conditions: geothermometry and oxygen barometry

Temperature and fO_2 were calculated with the thermobarometer of Andersen & Lindsley (1988) using the molecular fractions of ulvöspinel and ilmenite calculated by the method of Stormer (1983). Only homogeneous magnetite and ilmenite pairs in contact with groundmass that satisfy the empirical Mg/Mn partitioning test of Bacon & Hirschmann (1988) were used. High-Ti magnetite rims related to late diffusion and small Ti-rich grains from Lomas Limpias dacite were not used, to avoid invalid estimates (Devine *et al.*, 2003). Calculations were made using the ILMAT spreadsheet (Lepage, 2003). Coexisting amphibole–plagioclase pairs have been also used for thermometric calculations using the edenite–richterite formulation of Holland & Blundy (1994) for mineral pairs from dacites and mafic enclaves.

Magnetite–ilmenite pairs from Río Blanco pumices record redox conditions and temperatures of NNO +1·6 to +1·7 and 861 ± 21 °C, whereas amphibole–plagioclase pairs yield slightly lower temperatures of 824 ± 15 °C (Fig. 11; Supplementary Data). Similar oxidizing conditions of NNO +1·5 to +1·6 and 865 ± 31 °C are recorded by oxides in Lomas Limpias dacite, although higher temperatures of 931 ± 11 °C are estimated with high-Al amphibole–plagioclase pairs. Assuming that low-Al amphiboles were in equilibrium with plagioclase rims leads to lower and concordant values of 843 ± 20 °C.

As the reliability of fO_2 estimated by application of current formulations of the Fe–Ti oxide thermobarometers decreases above NNO + 1 (Rutherford & Devine, 1996; Evans & Scaillet, 1997; Scaillet & Evans, 1999), the use of corroborating methods is advisable. On the basis of the mole fraction of $FeSiO_3$ in orthopyroxene microphenocrysts ($X_{Fs} = 0{\cdot}25$–$0{\cdot}27$ in Río Blanco dacite; $X_{Fs} = 0{\cdot}30$–$0{\cdot}31$ in Lomas Limpias dacite), and considering the experimental results of Evans & Ghiorso (1995), we have estimated redox conditions of NNO + 1·7 and NNO + 1·5 in the Río Blanco and Lomas Limpias dacites. These values are similar to those obtained with Fe–Ti oxides, thereby corroborating the highly oxidizing conditions in NLV Holocene dacitic magmas. These results are also closely comparable with those reported for the Pinatubo 1991 (Evans & Scaillet, 1997) and Mount St. Helens 1980 (Rutherford & Devine, 1988) dacites, which have also adakitic signatures and include abundant amphibole phenocrysts (Cashman & Taggart, 1983; Bernard *et al.*, 1996). This result is also supported independently by magnetite compositions, which are in close agreement with those obtained in experiments at oxygen fugacities above NNO + 1 (Martel *et al.*, 1999).

Quench temperatures of 893 ± 28 °C were estimated from high-Al amphibole–plagioclase pairs in the least evolved enclaves (53·3–53·8 wt% SiO_2), which contain magnetite without ilmenite. Slightly lower values of 856 ± 6 °C and oxygen fugacities of NNO + 1·7, which are close to those in the host Lomas Limpias dacite, are recorded by Fe–Ti oxide pairs in two-oxide bearing enclaves (>54 wt% SiO_2). As olivine phenocrysts appear to be in equilibrium with the whole-rock compositions of the host enclaves, the Sack & Ghiorso (1991) formulation

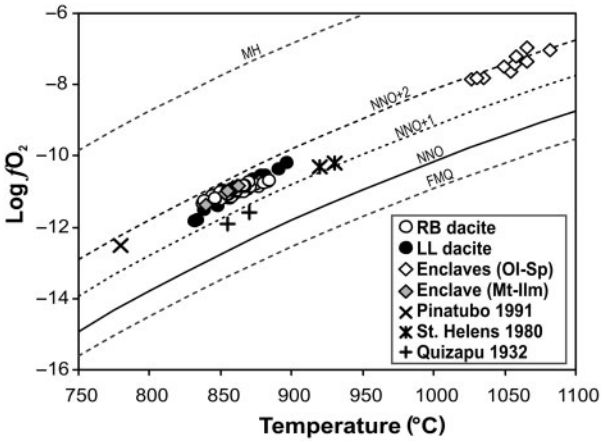

Fig. 11. Temperature vs fO_2 conditions of Holocene NLV magmas. Values were calculated using magnetite–ilmenite pairs (LL and RB dacites and enclaves) and spinel–olivine pairs (enclaves) (see text for details). Oxygen buffer curves: MH, magnetite–hematite; NNO, nickel–nickel oxide; FMQ, fayalite–magnetite–quartz. T–fO_2 conditions of some relevant dacites are included for comparison: Pinatubo dacite (1991) from Evans & Scaillet (1997); Mount St. Helens 1980 from Rutherford & Devine (1988); Quizapu 1932 from Hildreth & Drake (1992).

for coexisting olivine–spinel pairs has been used to derive a pre-injection liquidus temperature estimate of $1050 \pm 17^{\circ}C$ (assuming a pressure of 250 MPa). The same olivine–spinel pairs record highly oxidizing conditions of NNO + 1·9 to 2·3 on the basis of the Ballhaus *et al.* (1990, 1991, 1994) formulation (Supplementary Data). Although this oxygen barometer is ideally applied to more magnesian olivine compositions, wherein there also is coexisting orthopyroxene, it gives reasonable results for systems not saturated in this mineral. As minor corrections for the absence of orthopyroxene (<0·2 log units) do not significantly affect the estimated range, no correction has been applied (orthopyroxene is a late-crystallizing phase in enclaves).

Inferred pressures and water contents

No direct estimates of the pre-eruptive pressure conditions of NLV dacites are currently possible. Aluminum-in-hornblende barometry cannot be applied because of the absence of alkali feldspar and quartz in these rocks. Nevertheless, experimental data obtained from similar dacitic rocks provide indirect constraints on pressure and water content. Experimental phase relations at 200–220 MPa and water contents in the range 5–6 wt% for Pinatubo (1991) and Holocene San Pedro dacites (Scaillet & Evans, 1999; Costa *et al.*, 2004) reproduce the mineral assemblages in NLV dacites (plag + amph + opx + Fe–Ti ox) over the temperature range calculated from Fe–Ti oxide and plagioclase–amphibole thermometry (820–870°C). The prevalent core compositions of plagioclase phenocrysts in NLV dacites ($An_{30–45}$) are consistent with experimental results at ~5–6 wt% H_2O. Less common plagioclase phenocrysts or antecrysts with more calcic cores (up to An_{58}), may indicate higher temperatures and/or higher water contents in precursor magmas (Scaillet & Evans, 1999; Costa *et al.*, 2004).

The absence of clinopyroxene in NLV dacites mimics the absence of this phase in these experiments over the range of relevant temperatures. Maximum pressures for storage of the NLV dacitic magmas are constrained to be less than 400 MPa by experiments on Pinatubo (1991) dacite, as clinopyroxene appears as a stable phase at this pressure in proportions comparable with those of orthopyroxene (Prouteau & Scaillet, 2003). Clinopyroxene is also absent to rare in mafic enclaves and hornblende-rich cumulate xenoliths. Hornblende was evidently the dominant ferromagnesian mineral phase in many late eruptive products from NLV (Holocene and some pre-Holocene magmas).

The water contents of quenched mafic enclave magmas are constrained by experimental phase equilibria in basaltic to basaltic andesitic liquids. The stability of amphibole in such melts requires 5–6 wt% H_2O at pressures between 200 and 400 MPa (Sisson & Grove, 1993; Moore & Carmichael, 1998; Pichavant *et al.*, 2002; Barclay & Carmichael, 2004). Thus, a water content of ~5·5 wt% H_2O is inferred for these quenched mafic melts. The absence of marginal decompression-related reactions affecting amphiboles indicates that the ascent of dacitic magmas to the surface was sufficiently rapid to prevent the breakdown of amphibole (Rutherford & Hill, 1993).

Anomalous evolved magma compositions

The highly wet and oxidized dacitic magmas that were erupted from Nevado de Longaví during the Holocene, which are characterized by the combination of an adakitic signature and low incompatible element contents, are anomalous with respect to along-arc trends of the SVZ. Nonetheless, their Sr and Nd isotopic compositions are similar to those of magmas at neighboring volcanoes (Fig. 2). NLV dacites have concentrations of K and incompatible trace elements (with respect to low-pressure anhydrous mineral assemblages oliv + plag + pyx + ox) that are much lower than those of magmas in the northern SVZ magmas (34·5–33°S), for which isotopic data are consistent with significant crustal contributions (e.g. Tupungato magmas, Hildreth & Moorbath, 1988). Even more striking is the fact that these incompatible elements are lower in evolved NLV magmas than in comparable magmas that have ascended through thinner and apparently more refractory crust at centers well to the south of 36°S (Fig. 8a), where the main mechanism of evolution is thought to be nearly closed-system shallow-pressure fractionation (e.g. Gerlach *et al.*, 1988). These observations suggest that the mechanisms of generation of evolved magmas at NLV are different from those that predominate in other centers along the arc, and that upper crustal assimilation cannot have played a major role.

These unusually low incompatible element concentrations are coupled with La/Yb and Sr/Y ratios that are much higher than those in similarly evolved lavas at neighboring volcanoes, particularly those further to the south. The northernmost volcanoes in the SVZ, where the crust is significantly thicker than it is beneath the arc at 36·2°S, have comparably high ratios and relatively high Sr, but much higher concentrations of K, LREE, Rb, Th, Ba, and HFSE. Concentrations of Y and HREE are not so much strongly depleted at these northern cones, as they are more or less equivalent to the concentrations in the most mafic andesites. The high-La/Yb 'garnet signature' identified by Hildreth & Moorbath (1988) is accompanied by high $^{87}Sr/^{86}Sr$, low $^{143}Nd/^{144}Nd$, and high incompatible element contents (Fig. 2), and they interpreted this combination of features as the consequence of magmatic crustal assimilation and fractional crystallization at high pressure (MASH). Increasing Sr/Y and La/Yb with increasing SiO_2 at NLV are largely due to partitioning of Y and HREE into mineral phases (Fig. 9d and f) and not to selective LREE enrichment as a result of assimilation of high-pressure crustal components (Fig. 8b). These fundamental distinctions between NLV adakitic magmas and superficially similar silicic andesites and dacites that dominate some volcanoes in the northernmost SVZ pose questions about which processes and components were implicated in the genesis of the NLV adakites.

One general explanation for increasing La/Yb with increasing silica could be that high-La/Yb dacitic magmas generated by partial melting of the crust have been mixed with mantle-derived basalts. As the isotopic compositions of NLV adakitic magmas and mafic enclaves overlap, only young underplated mafic plutonic rocks are permitted as the sources of such melts. Some mixing, or back-mixing, of dacitic and more mafic magmas has occurred and this is most obviously manifested by the hybrid Castillo Andesite (Rodríguez, 2006), and in some pre-Holocene andesites that contain both hornblende and olivine with disequilibrium textures (Sellés, 2006). Nevertheless, petrographic evidence of mixing is lacking in NLV dacites, and a dominant role for melting and mixing is called into question by the fact that Al_2O_3, Sr, MgO, and Na_2O do not define linear arrays but rather display 'kinks' at about 57 wt% SiO_2 (Fig. 7e and 9b). Moreover, trace element ratios that are not substantially modified during fractionation of most igneous minerals, such as Nb/Zr (Fig. 9c), Nb/La, and Zr/La, are essentially constant from mafic to dacitic magmas. As such ratios are unlikely to be identical in mantle-derived basalts and melts derived from high-pressure melting of the lower crust, two-component mixing would not lead to these observations.

The incompatible element-poor nature of the Holocene dacites places additional constraints on the origin of these magmas. The generation of a melt with the low incompatible element concentrations of the Holocene NLV dacites by a realistic amount of melting (5–20%) of mafic arc crust (Rapp & Watson, 1995; Petford & Gallagher, 2001; Dufek & Bergantz, 2005; Annen *et al.*, 2006) would require a source whose incompatible trace element abundances were one-half to one-tenth of those in Rudnick & Gao's (2003) estimated lower crustal composition. Even if we were to accept the existence of such a depleted source, presumably dominated by ultramafic cumulates, an explanation of why this source is uniquely spatially related to NLV would be required.

A crystal fractionation model

An alternative hypothesis is that NLV adakitic dacites are products of differentiation of mafic magmas that are represented by the intimately associated quenched enclaves. The same restricted range of Nd and Sr isotopic compositions is shared by mafic and evolved magmas. Similarly highly oxidizing conditions (NNO + 1·7) are recorded by Fe–Ti oxides in the dacites, late-crystallizing oxides in the mafic enclaves, and early-crystallized olivine–spinel pairs. The mineralogy of the dacites and mafic enclaves is nearly the same, except for the occurrence of minor olivine phenocrysts in the most mafic samples. Hornblende and plagioclase with partly overlapping compositions dominate the mineral assemblages of enclaves and dacites, although their relative proportions change progressively. A co-genetic relationship is permitted by all these observations.

We have constrained the mineral assemblage(s) that may be involved in the generation of adakite-like dacites as a function of closed-system fractionation by major element mass-balance (Fig. 12) and trace element Rayleigh fractionation models (Fig. 13). In response to inflections in some major element trends near 57 wt% SiO_2 (e.g. Al_2O_3, Na_2O, Mg-number) we have adopted a two-stage, polybaric approach wherein the final product of the deeper, early stage of evolution is the starting composition for subsequent lower pressure fractionation.

The initial stage of fractionation was modeled using the most mafic enclave composition as the parental magma, from which averaged compositions of minerals in enclaves and amphibole gabbros were subtracted (Model A in Figs 12 and 13). The mineral proportions that minimize the residuals from 53 to 58 wt% SiO_2 are given in Table 5. Extraction of 30% (by mass) of an assemblage dominated by high-Al amphibole and calcic plagioclase reproduces the main compositional trends defined by the mafic enclaves, including early increases in Al_2O_3 and K_2O (Fig. 12; Table 5). The model mineral proportions, which are in reasonable agreement with observed mineral proportions, were used to calculate the trace element composition of the model evolved liquid. The mineral–melt partition coefficients used in this exercise were

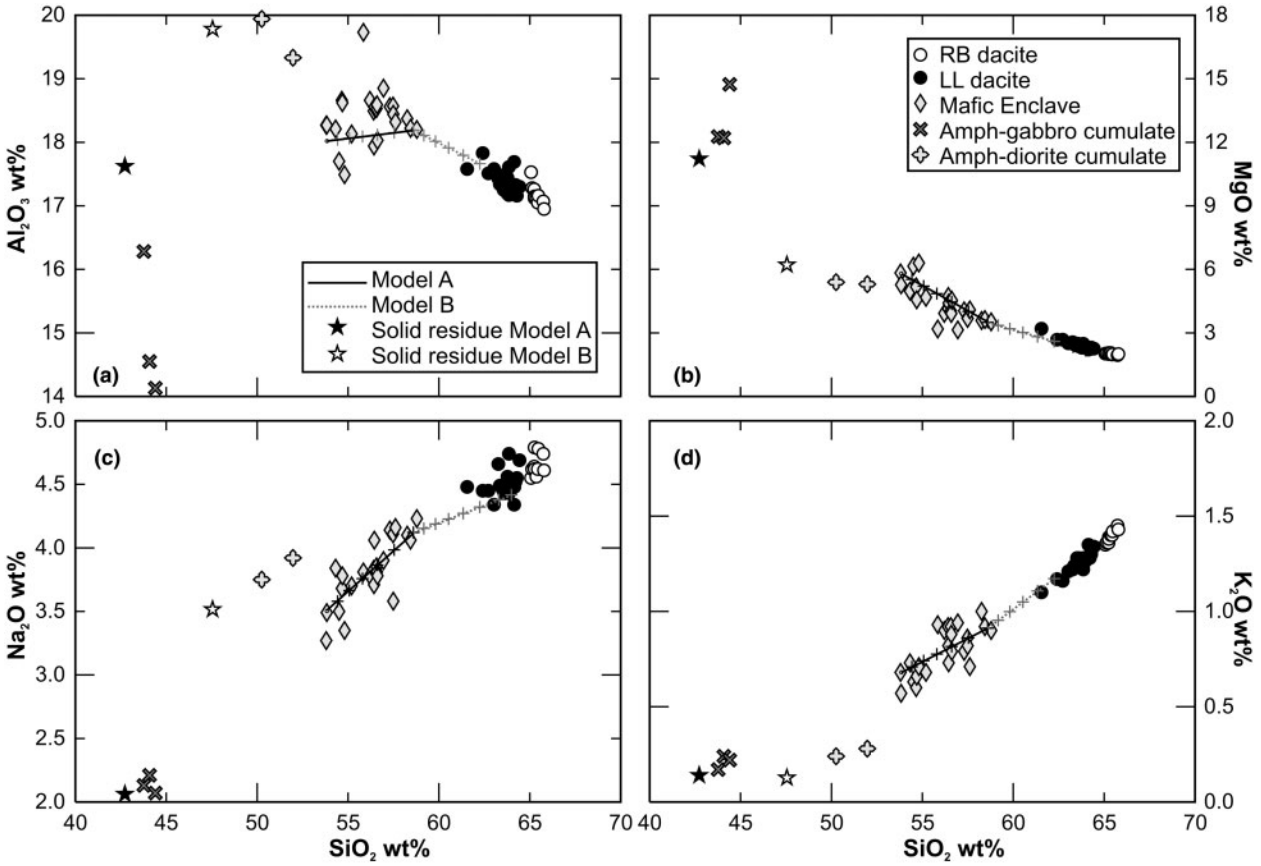

Fig. 12. Variation of Al_2O_3 (a), MgO (b), Na_2O (c) and K_2O (d) vs wt% SiO_2 showing the major element mass-balance models. Model A describes the early high-pressure trend defined by mafic to andesitic enclaves, whereas Model B corresponds to subsequent evolution towards more evolved magmas. Tick marks correspond to 5% fractionation.

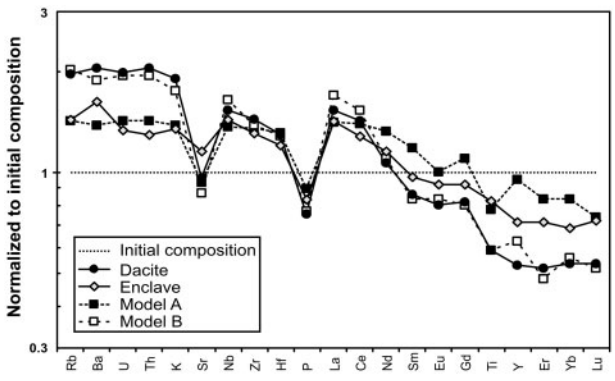

Fig. 13. Trace element Rayleigh fractional crystallization model results compared with natural samples. The end-product of Model A is compared with sample 7134 (an evolved enclave), and the final result of the second stage (Model B) is compared with a representative dacite (sample 7152). Values are normalized to the enclave used as the parent magma for the trace element model (sample 8704).

determined experimentally on water-rich basalts (J. Blundy, personal communication). In addition to the mineral phases that are observed in the enclaves and in other NLV mafic lavas, garnet was subtracted (1·5%) until the concentration of Lu in the model matched the concentration in the most evolved enclave.

The evolutionary stage from ~58 to 64 wt% SiO_2 is reproduced by a second increment of 33% fractionation (Model B) from the model liquid composition calculated in Model A (i.e. 53% total fractionation from the original parental liquid). The proportions and compositions of the fractionated minerals were changed to conform to the assemblages observed in evolved magmas, such as low-Al amphibole, intermediate plagioclase (~An_{55}), and low-Mg orthopyroxene (Table 6). The proportion of apatite in the fractionating mineral assemblage (0·68%) was determined by subtracting apatite until the concentration of P_2O_5 in the model liquid matched the concentration in the most evolved dacite. Calculated trace element concentrations reflect the consequences of apatite fractionation (Table 7). Trace elements were modeled using the partition coefficients in Table 8.

The solid assemblages of these two modeled stages of differentiation correspond very closely to the two types of cumulate-textured xenoliths previously described. The calculated solid residue of Model A is similar to the

Table 5: Parameters of mass-balance Model A

	Minerals							Mass balance				
	Amph	Plag	Ol	Cpx	Opx	Fe–Ti ox.	Gt	Parent	Model A	Enclave	Residuals	Model A
Proportion:	54·94	29·7	3·8	2·3	3·98	3·85	1·5		C_{fA}	7134	r	Solid residue
wt%												
SiO_2	43·07	45·7	38·8	51	53·4	0·13		53·78	58·57	58·44	–0·12	42·73
TiO_2	2·36		0·02	0·7	0·23	9·78		1·02	0·76	0·81	0·05	1·62
Al_2O_3	12·68	33·6	0·02	3·3	0·94	2·68		18	18·18	18·22	0·04	17·62
FeO*	11·38	0·46	20·8	7·6	17·8	77·14		7·5	6·02	6·1	0·08	12·19
MnO	0·16		0·34	0·3	0·67	0·4		0·13	0·11	0·11	0	0·15
MgO	14·4	0·18	40·3	15	24·9	2·5		5·8	3·49	3·63	0·14	11·21
CaO	11·7	17·2	0·14	21	1·18	0		8·5	6·9	6·85	–0·04	12·27
Na_2O	2·83	1·56	0	0·4	0·03	0		3·5	4·12	4·06	–0·05	2·06
K_2O	0·24	0·03						0·68	0·91	0·92	0·01	0·14
Cr_2O_3	0·12		0·01	0·2	0·01	0·61						
NiO			0·13	0	0							
Total	98·93	98·8	101	99	99·2	93·24						
Mg-no.	0·69		0·78	0·8	0·71	0·05					$\Sigma r^2 = 0.05$	
An (mol%)		85·7										

*Total iron as FeO.
Mineral proportions (wt%) calculated by least-squares optimization. Mineral compositions are averages of natural minerals in enclaves and cumulate xenoliths. Amph, amphibole; Plag, plagioclase; Ol, olivine; Cpx, clinopyroxene; Opx, orthopyroxene; Gt, garnet (not included in major element mass balance); C_f A, final composition with fraction of melt remaining = 0·7. Mg-number = Mg/(Mg + Fe*).

bulk composition of amphibole gabbro cumulates (Fig. 12; Table 5). Al_2O_3 contents show the largest mismatch because our calculations were based on reproducing the composition of a specific sample rather that the overall trend. Amphibole gabbros contain all the phases (except garnet) required to explain the main trend of evolution at the mafic end of the spectrum (Model A), including the large amounts of high-Al amphibole and calcic plagioclase. The proportions of olivine and pyroxenes required by Model A are higher than the modal abundances of these phases in amphibole gabbro cumulates, but the rounded shape of these minerals is textural evidence that they could have reacted with the liquid to form amphibole, as has been experimentally determined (e.g. Alonso-Pérez, 2006; Alonso-Pérez *et al.*, in preparation). Hence, the observed olivine and pyroxene proportions are minima.

The solid residue calculated for Model B closely resembles the composition of amphibole diorite cumulates, although at lower bulk SiO_2 (Table 6). This reflects the fact that the natural dioritic cumulates are probably residues from the crystallization of dacites, as is suggested by the coincidence in opx composition (Fig. 6), whereas Model B extends back to andesitic starting compositions. The calculated mineral association and proportion required to accomplish Model B also correspond closely to the mineralogy of the amphibole diorite cumulates. Quartz and biotite, which are present in the dioritic cumulates, but not in the dacites, are post-cumulus phases that appear in experiments at 220 MPa and ~50°C below the temperature recorded by Fe–Ti oxides in the dacites (Scaillet & Evans, 1999). We acknowledge that this model probably is a simplification. More rigorous fractional crystallization models would require experimental data at high pressures and high water contents that are, for the most part, still lacking, but there is no compelling evidence that a model with substantially greater complexity is required.

Evidence for garnet fractionation

The inference that cryptic garnet was a fractionating phase in the early evolution of water-rich mafic NLV magmas is based almost entirely on garnet's high partition coefficients for HREE and Y. Bulk partition coefficients for HREE and Y between 2·45 and 3·2 are needed to explain the observed depletions between 53 and 58 wt% SiO_2. If amphibole (~55 wt% of the fractionated assemblage) were the only phase to significantly retain HREE and Y, amphibole–melt partition coefficients of ~4·5–5·8 would

Table 6: Parameters of mass-balance Model B

	Minerals					Mass balance				
	Amph	Plag	Opx	Fe–Ti ox.	Ap	Parent	Model B	LL dacite	Residuals	Model B
Proportion:	34·07	56·5	2·92	5·84	0·7	C_f A	C_f B	7152	r	Solid residue
wt%										
SiO_2	44·94	53·8	53·3	0·12	0·29	58·57	64·13	64·05	−0·08	47·55
TiO_2	1·59		0·19	8·35		0·76	0·58	0·58	0	1·14
Al_2O_3	8·89	29·1	1·59	2·85	0·08	18·18	17·45	17·18	−0·27	19·78
FeO*	11·66	0·37	17·8	81·93	1·56	6·02	4·31	4·29	−0·02	10·61
MnO	0·28		0·96	0·4	0·12	0·11	0·1	0·09	−0·01	0·15
MgO	15·74	0·03	25·2	0·91	0·27	3·49	2·17	2·27	0·1	6·21
CaO	10·8	11·5	0·44		54·4	6·9	5·09	4·97	−0·12	10·64
Na_2O	1·86	5·06	0·02			4·12	4·43	4·48	0·05	3·51
K_2O	0·21	0·1				0·91	1·3	1·29	−0·01	0·13
P_2O_5					40·4	0·21	0·18	0·18	0	0·28
Total	95·97	100	99·5	94·56	97·1					
Mg-no.	0·71		0·72						$\Sigma r^2 = 0{\cdot}08$	
An (mol%)		55·4								

*Total iron as FeO.
Starting composition corresponds to the final composition of Model A (C_f A). Mineral proportions (wt%) calculated by least-squares optimization. Mineral compositions are averages of natural minerals. Amph, amphibole; Plag, plagioclase; Opx, orthopyroxene; Ap, apatite; C_f B, final composition with fraction of melt remaining = 0·67. Mg-number = Mg/(Mg + Fe*).

be required. Experimentally determined partition coefficients for amphibole in basaltic to basaltic andesitic liquids are of the order of 0·2 to <2 (Dalpé & Baker, 2000, and references therein). Even this level of uncertainty does not eliminate the need for garnet fractionation if our inferences about parental magmas are correct. HREE and Y depletions in intermediate to evolved liquids (58–65 wt% SiO_2) do not require garnet because partitioning of these elements into amphibole increases with increasing evolution. The partition coefficients needed to explain HREE and Y depletions in the second stage of the Rayleigh fractionation model are consistent with the ranges of published values for amphiboles in evolved magmas (Table 8).

This change from a garnet-assisted to an amphibole-driven increase in the La/Yb of evolved magmas also can be inferred from the geometry of chondrite-normalized REE patterns (Fig. 14). Amphibole fractionation tends to produce REE patterns that are concave upwards ('spoon'-shaped) because of the affinity of calcic amphiboles for the MREE (Gd to Ho) over the HREE (Er to Lu) (Klein *et al.*, 1997; Bottazzi *et al.*, 1999; Dalpé & Baker, 2000). Such concave patterns are not produced by garnet fractionation alone, which has much greater affinities for HREE. Amphibole fractionation produces derivative liquids with higher La/Yb than their parental magmas, but with lower MREE/HREE (e.g. Dy/Yb) unless another phase (such as garnet) participates in extracting HREE.

The low La/Yb and Dy/Yb of the most mafic enclaves at NLV are similar to the values for other basaltic magmas from the SVZ, and both of these ratios initially increase with increasing differentiation (Fig. 15). Such a trend cannot be produced by fractionation of amphibole alone as is directly shown by the high Dy/Yb of amphibole-rich cumulates, which can be taken as an approximation to the composition of high-Al amphiboles that were extracted from the mafic magmas. The trend changes from positively to negatively correlated at about 57–59 wt% SiO_2. This second leg of the trend is aligned with the composition of the amphibole diorite cumulates, compositional proxies for the residues extracted from intermediate to evolved magmas.

A small proportion of garnet (1·5%) in combination with a large amount of amphibole fractionation is needed to account for the REE chemistry of NLV magmas. Crystallization experiments on hydrous basalts at relatively oxidizing conditions have shown that garnet, in addition to amphibole, becomes a primary igneous phase at high H_2O contents at pressures between 1500 and 800 MPa, which is approximately the range of lower crustal pressures expected beneath NLV (Müntener *et al.*,

Table 7: Results of Rayleigh crystal fractionation Models A and B (C_f A and C_f B)

Element	Parent 8704	Model A C_f A	Model B C_f B	Enclave 7134	LL dacite 7152
ppm					
Rb	12·1	17·2	24·3	17·4	23·0
Ba	216	298	405	350	447
U	0·26	0·37	0·54	0·34	0·50
Th	0·92	1·31	1·81	1·19	1·44
K	5646	7745	9872	7617	10698
Sr	518	484	450	653	510
Nb	2·43	3·3	3·99	3·48	3·93
Zr	83	112	129	117	127
Hf	1·89	2·46	2·88	2·27	2·46
La	7·87	11·02	13·36	11·2	11·55
Ce	18·8	26·01	28·65	24·16	24·01
Nd	11·79	15·56	12·89	13·69	13·16
Sm	2·95	3·49	2·46	2·85	2·49
Eu	1·04	1·04	0·87	0·96	0·84
Gd	3·04	3·32	2·42	2·79	2·62
Ti	5933	4576	3491	4872	3479
Y	16·2	15·4	10·1	11·5	8·6
Er	1·5	1·25	0·74	1·07	0·78
Yb	1·4	1·16	0·82	0·95	0·75
Lu	0·21	0·16	0·12	0·15	0·11

Natural samples 7134 and 7152 are given for ease of comparison.

Table 8: Partition coefficients for intermediate to evolved melts used in the Rayleigh fractional crystallization model B

Element	D^{amph}_{melt}	D^{plag}_{melt}	D^{opx}_{melt}	D^{mt}_{melt}	D^{ap}_{melt}
Rb	0·29[10]	0·053[5]	0·022[5]	0·01[3]	
Ba	0·436[9]	0·160[5]	0·013[5]	0·01[3]	
U	0·10[10]				
Th	0·50[11]	0·01[5]	0·050[3]	0·10[3]	
K	0·96[2]	0·12[5]	0·014[5]	0·01[3]	
Sr	0·46[2]	1·600[5]	0·032[5]	0·01[3]	1·1[12]
Nb	1·30[4]	0·025[4]	0·350[5]	1·00[3]	
Zr	1·798[10]	0·010[5]	0·100[3]	0·20[3]	0·64[1]
Hf	1·731[6]	0·015[4]	0·100[3]		0·73[1]
La	0·72[6] (0·26–1·92)*	0·302[6]	0·031[6]		14·5[1]
Ce	1·11[6] (0·63–4·23)*	0·221[6]	0·028[6]	0·20[3]	34·7[2]
Nd	2·89[2] (1·24–8·7)*	0·149[6]	0·028[6]		57·1[2]
Sm	3·99[2] (2·22–7·76)*	0·102[6]	0·028[6]	0·30[3]	62·8[2]
Eu	3·44[2] (1·90–5·14)*	0·079[8]	0·028[6]	0·25[3]	30·4[2]
Gd	2·543[6] (2·54–10)*	0·056[8]	0·039[6]		56·3[2]
Ti	7[4]	0·050[4]	0·250[6]	12·5[2]	0·1[2]
Y	5[10] (2·46–11)*	0·060[4]	0·450[6]	0·50[4]	40[2]
Er	5·94[2] (1·98–8·2)*	0·045[6]	0·153[6]		37·2[2]
Yb	4·89[2] (0·31–5·5)*	0·041[6]	0·254[6]	0·25[3]	23·9[2]
Lu	4·53[2] (1·8–5·5)*	0·039[6]	0·323[6]		20·2[2]

*For REE preferred value and range of published partition coefficients are given.
References: 1, Fujimaki (1986); 2, Arth (1976); 3, Gill (1981); 4, Pearce & Norry (1979); 5, Philpotts & Schnetzler (1970) and Schnetzler & Philpotts (1970); 6, Fujimaki *et al.* (1984); 7, Green & Pearson (1983); 8, Drake & Weill (1975); 9, Matsui *et al.* (1977); 10, Ewart & Griffin (1994); 11, Dostal *et al.* (1983); 12, Watson & Green (1981).

2001; Alonso-Pérez, 2006; Alonso-Pérez *et al.*, in preparation). La/Yb in NLV dacites (~20) is among the highest within the SVZ, but this is a rather modest value with respect to the global adakitic dataset. Slightly higher percentages of residual garnet can have dramatic consequences on the REE of evolved magmas, and may account for greater depletions of HREE and Y elsewhere.

Water-rich mafic melts

High-Al amphiboles, which are by far the dominant type in mafic enclaves and amphibole gabbros, have been crystallized in experiments on mafic calc-alkaline starting materials at various pressures, and under water-rich to water-saturated conditions (Fig. 5), either as a liquidus phase or following olivine and augite (Sisson & Grove, 1993; Moore & Carmichael, 1998; Hilyard *et al.*, 2000; Müntener *et al.*, 2001; Pichavant *et al.*, 2002; Grove *et al.*, 2003, 2005). The Al^{IV} contents and the Si/Al^{total} ratio of experimental amphiboles ($P < 500$ MPa) is strongly controlled by the composition of the liquid, and most high-Al amphiboles coexist with liquids that have low SiO_2/Al_2O_3 ratios. Most of the high-Al-amphiboles in NLV lavas, enclaves and cumulate xenoliths could have crystallized directly from liquids with the bulk composition of mafic enclaves (Fig. 5e and f), whereas low-Al amphiboles are more consistent with crystallization from highly evolved residual melts. This is in keeping with the tendency of low-Al amphibole to occur as rims on high-Al cores of amphibole microphenocrysts. We infer that high-Al amphiboles in NLV magmas crystallized early from water-rich, mantle-derived parental magmas. The high Cr- and Mg-numbers of some high-Al amphiboles indicate that amphibole is an early phase in the crystallization sequence. The most magnesian NLV amphiboles (Mg-number = 0·78) could have precipitated from mafic magmas with as much as ~9 wt% H_2O (Grove *et al.*, 2005).

High-Al amphiboles coexist with An-rich plagioclase in amphibole gabbro cumulate xenoliths, which also suggests that the magma from which they crystallized was mafic

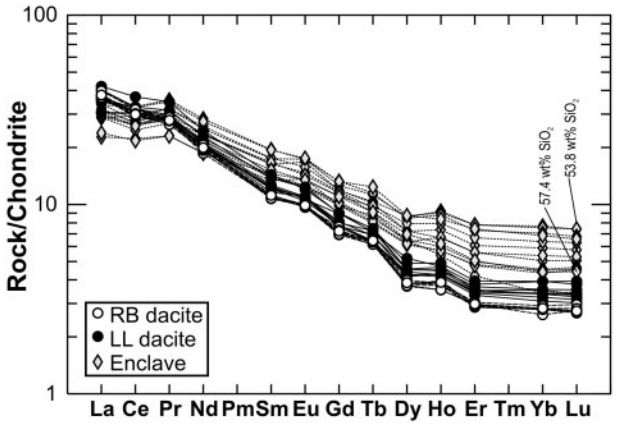

Fig. 14. Chondrite-normalized REE diagram (Nakamura, 1974) for Río Blanco (RB) and Lomas Limpias (LL) dacites and enclaves.

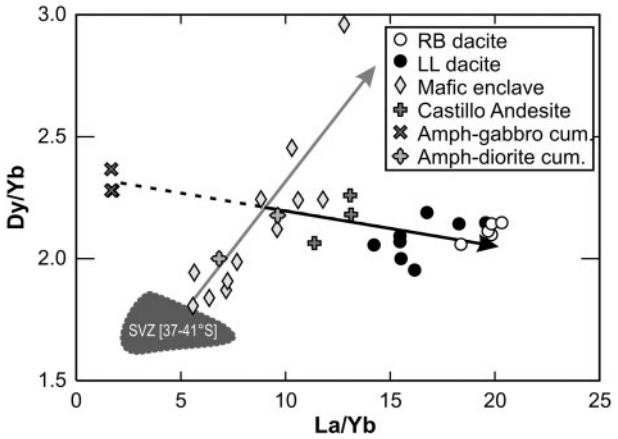

Fig. 15. Dy/Yb vs La/Yb variations throughout the compositional range of Holocene NLV magmas. The most mafic NLV enclaves are similar to other SVZ basalts in terms of these parameters (gray field), but the enclave trend is marked by increasing Dy/Yb and La/Yb, which cannot be produced by amphibole extraction alone. Garnet is inferred to have participated. In contrast, La/Yb increases towards dacite compositions without increasing Dy/Yb (continuous-line black arrow) are thought to be due to amphibole fractionation. The back-projection of this path to low La/Yb (dashed line) intersects the composition of an amphibole-rich cumulate.

and water-rich. The stability field of plagioclase contracts relative to ferromagnesian minerals and plagioclase becomes more calcic in progressively more water-rich magmas (e.g. Sisson & Grove, 1993). Near-liquidus crystallization experiments show that the An content of plagioclase increases almost linearly with increasing melt water content (Takagi *et al.*, 2005). Experimental results also show that plagioclase as calcic as $\sim An_{90}$ cannot crystallize from intermediate magmas under any P–T–H_2O condition because CaO and Al_2O_3 in the coexisting melt also play important roles (Panjasawatwong *et al.*, 1995). Water-rich mafic melts such as the NLV Holocene basaltic andesitic enclaves are appropriate for crystallization of the mineral phases in amphibole gabbros.

The fractionation of significant amounts of amphibole limits the rate of increase of incompatible element contents in evolved NLV magmas. Amphibole accommodates a number of elements that are highly incompatible with respect to anhydrous phases, thus retarding the development of high concentrations of these elements in residual liquids. More importantly, amphibole-rich + calcic plagioclase fractionating assemblages have lower bulk silica contents than dominantly pyroxene- and plagioclase-rich assemblages, thereby endowing an amphibole-rich assemblage with the potential to raise the silica content of derivative liquids at relatively low degrees of fractionation. Removal of 50% of an amphibole-rich assemblage implies that elements with bulk $D \sim 0$ will be enriched by a maximum factor of two ($F = 0{\cdot}5$), which is in good agreement with the observed enrichments for highly incompatible elements. Low-pressure fractionating assemblages such as those proposed for Villarrica volcano and the Planchón–Peteroa complex (Hickey-Vargas *et al.*, 1989; Tormey *et al.*, 1995), involving greater amounts of plagioclase, and pyroxenes and no amphibole, require 65–75% fractionation to achieve the same silica increase, and incompatible elements would be enriched by factors of 3–4.

No other center of the SVZ, with the possible exception of Calbuco volcano (Hickey-Vargas *et al.*, 1995; López-Escobar *et al.*, 1995*b*), appears to have erupted magmas with such an amphibole-rich mineralogy or an amphibole-dominated evolutionary path, from which we infer that magmas at NLV are particularly water-rich. This is consistent with the high boron contents in mafic to evolved lavas, and the elevated values for ratios indicative of fluid components (e.g. B/Zr, Ba/Th, Pb/Th) relative to other SVZ volcanic centers. We propose that locally elevated amounts of water-rich fluids flushed the mantle wedge beneath NLV, thereby inducing high degrees of mantle melting and the generation of water-rich primitive magmas. These water-rich magmas evolved along a fractionation path dominated by amphibole as the main ferromagnesian phase and reduced plagioclase stability, from which distinct evolved adakite-like magmas resulted.

The highly localized occurrence of wet magmas along the arc suggests that the source of fluids responsible for them is also a local anomaly. We postulate that serpentinite bodies hosted in the oceanic Mocha Fracture Zone, whose down-dip projection coincides with the location of NLV, are responsible for providing elevated amounts of fluids to the mantle wedge beneath NLV. Additional evidence to be presented elsewhere indicates that magmas erupted 1 Myr ago at the present location of NLV were not exceptionally wet, and evolved along paths that are typical for the SVZ (Sellés, 2006), which indicates that water flux has only recently been elevated. This is consistent with the southward along-arc migration of the fracture zone. Whether other adakite-like rocks exist in older,

more northerly sequences as a result of the passage of the fracture zone remains to be investigated.

SUMMARY AND IMPLICATIONS

The two Holocene dacitic episodes at NLV produced the most evolved magma compositions that are preserved at this volcano, although occurrences of amphibole-rich cumulate xenoliths in earlier main-cone lavas indicate that magmas lying along similar liquid lines of descent were being generated at depth by the NLV magmatic system prior to the Holocene (Sellés, 2006). The erupted dacites have adakitic signatures, high B and fluid-mobile/immobile trace element ratios, and amphibole-rich phenocryst assemblages, and they lack clinopyroxene. Quenched mafic enclaves in dacitic rocks represent inputs of unusually water-rich magmas, which also have relatively low concentrations of most incompatible elements, high B, high mobile/immobile trace element ratios, and a high modal proportion of amphibole phenocrysts. These similarities and their mingled association in the Lomas Limpias dacite and Castillo Andesite strongly support a close genetic link in the form of a parental role for the enclave magmas.

A polybaric, two-stage crystal extraction model constrained by experimentally determined phase relations and natural mineral compositions reproduces whole-rock major and trace element trends and is a logical consequence of differentiation of these extremely water-rich magmas. Anomalously low incompatible trace element concentrations in dacites (except for boron) are not consistent with significant upper crustal assimilation, but they are easily reconciled with volumetrically important fractionation of amphibole, which in turn is supported by the presence of amphibole-rich cumulate xenoliths. The trace element abundances in the early, high-pressure stage of evolution have been adjusted by the fractionation of 1·5% garnet. Although modal garnet is not observed, experimental studies (Müntener *et al.*, 200l; Ulmer & Müntener, 2005; Alonso-Pérez, 2006) have shown that it could be stable in wet mantle-derived melts at pressures corresponding to inferred lower crustal pressures below NLV. The lack of erupted primitive melts precludes rigorous modeling of the early, deep fractionation, which is inferred to be the key to the adakitic signature of the Holocene NLV magmas. The deep hot zone model proposed by Annen *et al.* (2006) provides an adequate thermo-mechanical framework for generation of magmas derived by fractionation of high-pressure assemblages from hydrous, mantle-derived magmas.

A crystal fractionation origin for adakite-like rocks has been proposed in earlier studies for other arc settings, notably in the geodynamically complex Philippine arc (Castillo *et al.*, 1999; Prouteau & Scaillet, 2003; Solidum *et al.*, 2003; Castillo & Newhall, 2004; Macpherson *et al.*, 2006), but also in the Ecuadorian Andes (Chiaradia *et al.*, 2004) and the Archean of South Africa (Kleinhanns *et al.*, 2003). All of these studies concur that amphibole plays a preponderant role in the generation of the adakitic signature (with or without garnet), as well as limiting the amount of plagioclase being fractionated. Previous studies call upon elevated magmatic water contents to explain the participation of amphibole-rich assemblages, although the reasons why elevated water fluxes occurred at a given place and time remain largely unexplored. We propose that this unique occurrence of adakitic magmas in the Quaternary Andean SVZ is ultimately related to the position of Nevado de Longaví above the down-dip projection of the oceanic Mocha Fracture Zone, which could transport large amounts of water hosted in serpentinite bodies (e.g. Bonatti & Crane, 1984; Ulmer & Trommdorff, 1995; Kerrick, 2002; Macleod *et al.*, 2002; Ranero *et al.*, 2003; Ranero & Sallarès, 2004).

ACKNOWLEDGEMENTS

This work was supported by Swiss Fonds National Grant 20-63950.00 and with the collaboration of Servicio Nacional de Geología y Minería SERNAGEOMIN-Chile. D. Sellés was supported during part of the project by the Swiss Confederation Fellowship. The manuscript has enormously benefited from the careful reviews by Peter Ulmer, Paterno Castillo and Colin Macpherson, as well as from the editorial handling by Wendy Bohrson. We would like to thank François Bussy and Georges Morris for granting access to the microprobe at Lausanne University and for providing extensive technical support, including during out-of-office time. Elizabeth Gier and Susan Woods are acknowledged for technical support during ICP-MS sample preparation and analysis at Harvard University. David Chew, Massimo Chiaradia and Dennis Fontignie are acknowledged for their valuable help and guidance during isotopic determinations, and Fabio Caponni for the XRF analyses. Our understanding of the subject has immensely benefited in recent years from extended discussions with Othmar Müntener and Jon Blundy, who also provided us with essential unpublished material.

SUPPLEMENTARY DATA

Supplementary data for this paper are available at *Journal of Petrology* online.

REFERENCES

Alonso-Pérez, R. (2006). The role of garnet in the evolution of hydrous, calcalkaline magmas: An experimental study at 0·8–1·5 GPa. Ph.D. thesis, Swiss Federal Institute of Technology, Zurich, 178 pp.

Andersen, D. & Lindsley, D. (1988). Internally consistent solution model for Fe-Mg-Mn-Ti oxides: Fe–Ti oxides. *American Mineralogist* **73**, 714–726.

Annen, C., Blundy, J. & Sparks, R. S. J. (2006). The genesis of intermediate and silicic magmas in deep crustal hot zones. *Journal of Petrology* **47**, 505–539.

Arth, J. G. (1976). Behavior of trace elements during magmatic processes: a summary of theoretical models and their applications. *Journal of Research of the US Geological Survey* **4**, 41–47.

Atherton, M. P. & Petford, N. (1993). Generation of sodium-rich magmas from newly underplated basaltic crust. *Nature* **362**, 144–146.

Atherton, M. P. & Petford, N. (1996). Plutonism and the growth of Andean crust at 9°S from 100 to 3 Ma. *Journal of South American Earth Sciences* **9**, 1–9.

Bacon, C. (1986). Magmatic inclusions in silicic and intermediate volcanic rocks. *Journal of Geophysical Research* **91**, 6091–6112.

Bacon, C. & Hirschmann, M. (1988). Mg/Mn partitioning as a test for equilibrium between coexisting Fe–Ti oxides. *American Mineralogist* **73**, 57–61.

Ballhaus, C., Berry, R. F. & Green, D. H. (1990). Oxygen fugacity controls in the Earth's upper mantle. *Nature* **348**, 437–440.

Ballhaus, C., Berry, R. & Green, D. (1991). High pressure experimental calibration of olivine–orthopyroxene–spinel oxygen geobarometer: implications for the oxidation state of the upper mantle. *Contributions to Mineralogy and Petrology* **107**, 27–40.

Ballhaus, C., Berry, R. F. & Green, D. H. (1994). Erratum. High-pressure experimental calibration of the olivine–orthopyroxene–spinel oxygen geobarometer: implications for the oxidation state of the upper mantle. *Contributions to Mineralogy and Petrology* **118**, 109.

Barclay, J. & Carmichael, I. S. E. (2004). A hornblende basalt from Western Mexico: water-saturated phase relations constrain a pressure–temperature window of eruptibility. *Journal of Petrology* **45**, 485–506.

Bernard, A., Knittel, U., Weber, B., Weis, D., Albrecht, A., Hattori, K., Klein, J. & Oles, D. (1996). Petrology and geochemistry of the 1991 eruption products of Mount Pinatubo. In: Newhall, C. G. & Punongbayan, R. S. (eds) *Fire and Mud: Eruptions and Lahars of Mount Pinatubo, Philippines*. Seattle, WA: University of Washington Press, Quezon City, Philippines: PHIVOLCS, pp. 767–797.

Bohm, M., Luth, S., Echtler, H., Asch, G., Bataille, K., Bruhn, C., Rietbrock, A. & Wigger, P. (2002). The Southern Andes between 36° and 40°S latitude: seismicity and average seismic velocities. *Tectonophysics* **356**, 275–289.

Bonatti, E. & Crane, K. (1984). Oceanic fracture zones. *Scientific American* **250**, 36–47.

Bottazzi, P., Tiepolo, M., Vannucci, R., Zanetti, A., Brumm, R., Foley, S. F. & Oberti, R. (1999). Distinct site preferences for heavy and light REE in amphibole and the prediction of Amph/LDREE. *Contributions to Mineralogy and Petrology* **137**, 36–45.

Cashman, K. V. & Taggart, J. E. (1983). Petrologic monitoring of 1981 and 1982 eruptive products from Mount St. Helens. *Science* **221**, 1385–1387.

Castillo, P. (2006). An overview of adakite petrogenesis. *Chinese Science Bulletin* **51**, 257–268.

Castillo, P. R. & Newhall, C. G. (2004). Geochemical constraints on possible subduction components in lavas of Mayon and Taal Volcanoes, Southern Luzon, Philippines. *Journal of Petrology* **45**, 1089–1108.

Castillo, P. R., Janney, P. E. & Solidum, R. U. (1999). Petrology and geochemistry of Camiguin Island, southern Philippines: insights to the source of adakites and other lavas in a complex arc setting. *Contributions to Mineralogy and Petrology* **134**, 33–51.

Chiaradia, M., Fontbote, L. & Beate, B. (2004). Cenozoic continental arc magmatism and associated mineralization in Ecuador. *Mineralium Deposita* **39**, 204–222.

Coombs, M. L., Eichelberger, J. C. & Rutherford, M. J. (2000). Magma storage and mixing conditions for the 1953–1974 eruptions of Southwest Trident volcano, Katmai National Park, Alaska. *Contributions to Mineralogy and Petrology* **140**, 99–118.

Costa, F. & Singer, B. (2002). Evolution of Holocene dacite and compositionally zoned magma, Volcán San Pedro, Southern Volcanic Zone, Chile. *Journal of Petrology* **43**, 1571–1593.

Costa, F., Dungan, M. A. & Singer, B. S. (2002). Hornblende- and phlogopite-bearing gabbroic xenoliths from Volcan San Pedro (36°S), Chilean Andes: evidence for melt and fluid migration and reactions in subduction-related plutons. *Journal of Petrology* **43**, 219–241.

Costa, F., Scaillet, B. & Pichavant, M. (2004). Petrological and experimental constraints on the pre-eruption conditions of Holocene dacite from Volcan San Pedro (36°S, Chilean Andes) and the importance of sulphur in silicic subduction-related magmas. *Journal of Petrology* **45**, 855–881.

Dalpé, C. & Baker, D. R. (2000). Experimental investigation of large-ion-lithophile-element-, high-field-strength-element- and rare-earth-element-partitioning between calcic amphibole and basaltic melt: the effects of pressure and oxygen fugacity. *Contributions to Mineralogy and Petrology* **140**, 233–250.

Davidson, J., Dungan, M., Ferguson, K. & Colucci, M. (1987). Crust–magma interactions and the evolution of arc magmas: The San Pedro–Pellado volcanic complex, southern Chilean Andes. *Geology* **15**, 443–446.

Defant, M. J. & Drummond, M. S. (1990). Derivation of some modern arc magmas by melting of young subducted lithosphere. *Nature* **347**, 662–665.

Déruelle, B., Harmon, R. & Moorbath, S. (1983). Sr–O isotope relationships and petrogenesis of Andean volcanics of South America. *Nature* **302**, 814–816.

Déruelle, B. & López-Escobar, L. (1999). Basaltes, andésites, dacites et rhyolites des stratovolcans des Nevados de Chillán et de l'Antuco (Andes méridionales): une remarquable illustration d'une différenciation par cristallisation fractionnée. *Comptes Rendus de l'Académie des Sciences, Sciences de la Terre et des Planètes* **329**, 337–344.

Devine, J. D., Rutherford, M. J., Norton, G. E. & Young, S. R. (2003). Magma storage region processes inferred from geochemistry of Fe–Ti oxides in andesitic magma, Soufrière Hills Volcano, Montserrat, W.I. *Journal of Petrology* **44**, 1375–1400.

Dixon, H. J., Murphy, M. D., Sparks, S. J., Chávez, R., Naranjo, J. A., Dunkley, P. N., Young, S. R., Gilbert, J. S. & Pringle, M. R. (1999). The geology of Nevados de Chillán volcano, Chile. *Revista Geológica de Chile* **26**, 227–253.

Dostal, J., Dupuy, C., Carron, J. P., Dekerneizon, M. L. & Maury, R. C. (1983). Partition coefficients of trace elements: Application to volcanic rocks of St. Vincent, West Indies. *Geochimica et Cosmochimica Acta* **47**, 525–533.

Drake, M. J. & Weill, D. F. (1975). Partition of Sr, Ba, Ca, Y, Eu^{2+}, Eu^{3+}, and other REE between plagioclase feldspar and magmatic liquid—experimental study. *Geochimica et Cosmochimica Acta* **39**, 689–712.

Dufek, J. & Bergantz, G. W. (2005). Lower crustal magma genesis and preservation: a stochastic framework for the evaluation of basalt–crust interaction. *Journal of Petrology* **46**, 2167–2195.

Dungan, M. A., Wulff, A. & Thomson, R. (2001). Eruptive stratigraphy of the Tatara–San Pedro Complex, 36°S, Southern Volcanic Zone, Chilean Andes: Reconstruction method and implications for magma evolution at long-lived arc volcanic centers. *Journal of Petrology* **42**, 555–626.

Evans, B. & Ghiorso, M. (1995). Thermodynamics and petrology of cummingtonite. *American Mineralogist* **80**, 649–663.

Evans, B. & Scaillet, B. (1997). The redox state of Pinatubo dacite and the ilmenite–hematite solvus. *American Mineralogist* **82**, 625–629.

Ewart, A. & Griffin, W. L. (1994). Application of proton-microprobe data to trace-element partitioning in volcanic rocks. *Chemical Geology* **117**, 251–284.

Ferguson, K., Dungan, M., Davidson, J. & Colucci, M. (1992). The Tatara–San Pedro Volcano, 36°S, Chile: A chemical variable, dominantly mafia magmatic system. *Journal of Petrology* **33**, 1–43.

Folguera, A., Ramos, V. A. & Melnick, D. (2002). Partición de la deformación en la zona del arco volcánico de los Andes neuquinos (36–39°S) en los últimos 30 millones de años. *Revista Geológica de Chile* **29**, 227–240.

Folguera, A., Ramos, V. A., Hermanns, R. L. & Naranjo, J. A. (2004). Neotectonics in the foothills of the southernmost central Andes (37°–38°S): Evidence of strike-slip displacement along the Antiñir–Copahue fault zone. *Tectonics* **23**, 1–23.

Fujimaki, H. (1986). Partition coefficients of Hf, Zr, and REE between zircon, apatite, and liquid. *Contributions to Mineralogy and Petrology* **94**, 42–45.

Fujimaki, H., Tatsumoto, M. & Aoki, K. (1984). Partition coefficients of Hf, Zr, and REE between phenocrysts and groundmasses. *Journal of Geophysical Research* **89**, 662–672.

Futa, K. & Stern, C. R. (1988). Sr and Nd isotopic and trace element compositions of Quaternary volcanic centers of the Southern Andes. *Earth and Planetary Science Letters* **88**, 253–262.

Garcia, M. O. & Jacobson, S. S. (1979). Crystal clots, amphibole fractionation and the evolution of calc-alkaline magmas. *Contributions to Mineralogy and Petrology* **69**, 319–327.

Gerlach, D., Frey, F., Moreno, H. & López-Escobar, L. (1988). Recent volcanism in the Puyehue–Cordón Caulle Region, Southern Andes, Chile (40·5°S): Petrogenesis of evolved lavas. *Journal of Petrology* **29**, 333–382.

Gill, J. B. (1981). *Orogenic Andesites and Plate Tectonics*. Berlin: Springer, 390 p.

Goss, A.R. & Kay, S. M. (2006). Steep REE patterns and enriched Pb isotopes in southern Central American arc magmas: Evidence for forearc subduction erosion? *Geochemistry, Geophysics, Geosystems* **7**, Q05016, doi:05010.01029/02005GC001163.

Green, T. H. & Pearson, N. J. (1983). Effect of pressure on rare earth element partition coefficients in common magmas. *Nature* **305**, 414–416.

Grove, T. L., Donnelly-Nolan, J. M. & Housh, T. (1997). Magmatic processes that generated the rhyolite of Glass Mountain, Medicine Lake volcano, N. California. *Contributions to Mineralogy and Petrology* **127**, 205–223.

Grove, T. L., Elkins-Tanton, L. T., Parman, S. W., Chatterjee, N., Müntener, O. & Gaetani, G. A. (2003). Fractional crystallization and mantle-melting controls on calc-alkaline differentiation trends. *Contributions to Mineralogy and Petrology* **145**, 515–533.

Grove, T. L., Baker, M. B., Price, R. C., Parman, S. W., Elkins-Tanton, L. T., Chatterjee, N. & Müntener, O. (2005). Magnesian andesite and dacite lavas from Mt. Shasta, northern California: products of fractional crystallization of H_2O-rich mantle melts. *Contributions to Mineralogy and Petrology* **148**, 542–565.

Gutscher, M., Maury, R., Eissen, J. & Bourdon, E. (2000). Can slab melting be caused by flat subduction? *Geology* **28**, 535–538.

Harmon, R., Barreiro, B., Moorbath, S., Hoefs, J., Francis, P., Thorpe, B., Deruelle, B., McHugh, J. & Viglino, J. (1984). Regional O-, Sr-, and Pb-isotope relationships in late Cenozoic calc-alkaline lavas of the Andean Cordillera. *Journal of Geological Society, London* **141**, 803–822.

Herron, E. (1981). Chile margin near lat. 388S: Evidence for a genetic relationship between continental and marine features or a cause of curious coincidences? In: Kulm, L.D., Dymond, J., Dasch, E.J. & Hussong, D.M. (eds) *Nazca Plate: Crustal formation and Andean convergence. Geological Society of America, Memoirs* **154**, 755–760.

Hickey, R. L., Gerlach, D. & Frey, F. (1984). Geochemical variations volcanic rocks from central–south Chile (33°–42°S): implications for their petrogenesis. In: Harmon, R. & Barreiro, B. (eds) *Andean Magmatism: Chemical and Isotopic Constraints*. Nantwich: Shiva, pp. 72–95.

Hickey, R. L., Frey, F. A., Gerlach, D. C. & López-Escobar, L. (1986). Multiple sources for basaltic arc rocks from the Southern Volcanic Zone of the Andes (34°–41°S): Trace element and isotopic evidence for contributions from subducted oceanic crust, mantle and continental crust. *Journal of Geophysical Research* **91**, 5963–5983.

Hickey-Vargas, R., Moreno, H., López-Escobar, L. & Frey, F. A. (1989). Geochemical variations in Andean basaltic and silicic lavas from the Villarrica–Lanin volcanic chain (39·5°S): an evaluation of source heterogeneity, fractional crystallization and crustal assimilation. *Contributions to Mineralogy and Petrology* **103**, 361–386.

Hickey-Vargas, R., Abdollahi, M. J., Parada, M. A., López-Escobar, L. & Frey, F. A. (1995). Crustal xenoliths from Calbuco Volcano, Andean Southern Volcanic Zone: implications for crustal composition and magma–crust interaction. *Contributions to Mineralogy and Petrology* **119**, 331–344.

Hildreth, W. & Drake, R. E. (1992). Volcán Quizapu, Chilean Andes. *Bulletin of Volcanology* **54**, 93–125.

Hildreth, W. & Moorbath, S. (1988). Crustal contributions to arc magmatism in the Andes of Central Chile. *Contributions to Mineralogy and Petrology* **98**, 455–489.

Hilyard, M., Nielsen, R. L., Beard, J. S., Patiño-Douce, A. & Blencoe, J. (2000). Experimental determination of the partitioning behavior of rare earth and high field strength elements between pargasitic amphibole and natural silicate melts. *Geochimica et Cosmochimica Acta* **64**, 1103–1120.

Holland, T. & Blundy, J. (1994). Non-ideal interactions in calcic amphiboles and their bearing on amphibole–plagioclase thermometry. *Contributions to Mineralogy and Petrology* **116**, 433–447.

Kay, R. W. (1978). Aleutian magnesian andesites: Melts from subducted Pacific Ocean crust. *Journal of Volcanology and Geothermal Research* **4**, 117–132.

Kay, S., Godoy, E. & Kurtz, A. (2005). Episodic arc migration, crustal thickening, subduction erosion, and magmatism in the south–central Andes. *Geological Society of America Bulletin* **117**, 67–88.

Kerrick, D. (2002). Serpentinite seduction. *Science* **298**, 1344–1345.

Klein, M., Stosch, H.-G. & Seck, H. A. (1997). Partitioning of high field-strength and rare-earth elements between amphibole and quartz-dioritic to tonalitic melts: an experimental study. *Chemical Geology* **138**, 257–271.

Kleinhanns, I., Kramers, J. & Kamber, B. (2003). Importance of water for Archaean granitoid petrology: a comparative study of TTG and potassic granitoids from Barberton Mountain Land, South Africa. *Contributions to Mineralogy and Petrology* **145**, 377–389.

Kley, J. & Monaldi, C. R. (1998). Tectonic shortening and crustal thickness in the Central Andes: How good is the correlation? *Geology* **26**, 723–726.

Kley, J., Monaldi, C. R. & Salfity, J. A. (1999). Along-strike segmentation of the Andean foreland: causes and consequences. *Tectonophysics* **301**, 75–94.

Leake, B., Woolley, A., Arps, C., Birch, W., Gilbert, M., Grice, J., Hawthorne, F., Kato, A., Kisch, H., Krivovichev, V., Linthout, K., Laird, J., Mandarino, J., Maresch, W., Nickel, E., Rock, N., Schumacher, J., Smith, D., Stephenson, N.,

Ungaretti, L., Whittaker, E. & Youzhi, G. (1997). Nomenclature of amphiboles: report of the subcommittee on amphiboles of the International Mineralogical Association, Commission on New Minerals and Minerals Names. *American Mineralogist* **82**, 1019–1037.

Lepage, L. (2003). ILMAT: an excel worksheet for ilmenite–magnetite geothermometry and geobarometry. *Computers and Geosciences* **29**, 673–678.

López-Escobar, L., Parada, M. A., Moreno, H., Frey, F. & Hickey-Vargas, R. (1992). A contribution to the petrogenesis of Osorno and Calbuco volcanoes, Southern Andes (41°00'–41°30'S): comparative study. *Revista Geológica de Chile* **19**, 211–226.

López-Escobar, L., Cembrano, J. & Moreno, H. (1995a). Geochemistry and tectonics of the Chilean Southern Andes basaltic Quaternary volcanism (37–46°S). *Revista Geológica de Chile* **22**, 219–234.

López-Escobar, L., Parada, M. A., Hickey-Vargas, R., Frey, F. A., Kempton, P. D. & Moreno, H. (1995b). Calbuco Volcano and minor eruptive centers distributed along the Liquiñe–Ofqui Fault Zone, Chile (41°–42°S): contrasting origin of andesitic and basaltic magma in the Southern Volcanic Zone of the Andes. *Contributions to Mineralogy and Petrology* **119**, 345–361.

Lucassen, F., Trumbull, R., Franz, G., Creixell, C., Vázquez, P., Romer, R. & Figueroa, O. (2004). Distinguishing crustal recycling and juvenile additions at active continental margins: the Paleozoic to recent compositional evolution of the Chilean Pacific margin (36–41°S). *Journal of South American Earth Sciences* **17**, 103–119.

Macleod, C. J., Escartín, J., Banerji, D., Banks, G. J., Gleeson, M., Irving, D. H. B., Lilly, R. M., Mccaig, A. M., Niu, Y., Allerton, S. & Smith, D. K. (2002). Direct geological evidence for oceanic detachment faulting: The Mid-Atlantic Ridge, 15°45′N. *Geology* **30**, 879–882.

Macpherson, C. G., Dreher, S. T. & Thirlwall, M. F. (2006). Adakites without slab melting: high pressure differentiation of island arc magma, Mindanao, the Philippines. *Earth and Planetary Science Letters* **243**, 581–593.

Martel, C., Pichavant, M., Holtz, F. & Scaillet, B. (1999). Effects of fO_2 and H_2O on andesite phase relations between 2 and 4 kbar. *Journal of Geophysical Research* **104**, 29453–29470.

Matsui, Y., Onuma, N., Nagasawa, H., Higuchi, H. & Banno, S. (1977). Crystal structure control in trace element partition between crystal and magma. *Tectonics* **100**, 315–324.

McMillan, N., Harmon, R., Moobath, S., López-Escobar, L. & Strong, D. (1989). Crustal sources involved in continental arc magmatism: A case study of Volcan Mocho–Choshuenco, southern Chile. *Geology* **17**, 1152–1156.

Moore, G. & Carmichael, I. S. E. (1998). The hydrous phase equilibria (to 3 kbar) of an andesite and basaltic andesite from western Mexico: constraints on water content and conditions of phenocryst growth. *Contributions to Mineralogy and Petrology* **130**, 304–319.

Muñoz, J. & Niemeyer, C. (1984). *Hoja Laguna del Maule, Regiones del Maule y del Bío Bío*. Carta Geológica de Chile No. 64, escala 1:250 000. Santiago: Servicio Nacional de Geología y Minería, p. 98.

Müntener, O., Kelemen, P. & Grove, T. (2001). The role of H_2O during crystallization of primitive arc magmas under uppermost mantle conditions and genesis of igneous pyroxenites: an experimental study. *Contributions to Mineralogy and Petrology* **141**, 643–658.

Nakamura, N. (1974). Determination of REE, Ba, Fe, Mg, Na and K in carbonaceous and ordinary chondrites. *Geochimica et Cosmochimica Acta* **38**, 757–775.

Nakamura, Y. & Kushiro, I. (1970). Compositional relations of coexisting orthopyroxene, pigeonite, and augite in a tholeiitic andesite from Hakone volcano. *Contributions to Mineralogy and Petrology* **26**, 265–275.

Nelson, S. T., Davidson, J. P., Heizler, M. T. & Kowallis, B. J. (1999). Tertiary tectonic history of the southern Andes: The subvolcanic sequence to the Tatara–San Pedro volcanic complex, lat 36°S. *Geological Society of America Bulletin* **111**, 1387–1404.

Panjasawatwong, Y., Danyushevsky, L. V., Crawford, A. J. & Harris, K. L. (1995). An experimental study of the effects of melt composition on plagioclase–melt equilibria at 5 and 10 kbar: implications for the origin of magmatic high-An plagioclase. *Contributions to Mineralogy and Petrology* **118**, 420–432.

Peacock, S. & Wang, K. (1999). Seismic consequences of warm versus cool subduction metamorphism: examples from Southwest and Northeast Japan. *Science* **286**, 937–939.

Pearce, J. A. & Norry, M. J. (1979). Petrogenetic implications of Ti, Zr, Y, and Nb variations in volcanic rocks. *Contributions to Mineralogy and Petrology* **69**, 33–47.

Petford, N. & Gallagher, K. (2001). Partial melting of mafic (amphibolitic) lower crust by periodic influx of basaltic magma. *Earth and Planetary Science Letters* **193**, 483–499.

Pfeifer, H. R., Lavanchy, J. C. & Serneels, V. (1991). Bulk chemical and industrial materials by X-Ray Fluorescence, recent developments and aplication to material rich in iron oxides. *Journal of Trace Microprobe Techniques* **9**, 127–147.

Philpotts, J. A. & Schnetzler, C. C. (1970). Phenocryst–matrix partition coefficients for K, Rb, Sr and Ba, with applications to anorthosite and basalt genesis. *Geochimica et Cosmochimica Acta* **34**, 307–322.

Pichavant, M., Martel, C., J., B. & Scaillet, B. (2002). Physical conditions, structure and dynamics of a zoned magma chamber: Mount Pelée (Martinique, Lesser Antilles Arc). *Journal of Geophysical Research* **107**, ECV 1-1–ECV 1-27.

Prouteau, G. & Scaillet, B. (2003). Experimental constraints on the origin of the 1991 Pinatubo dacite. *Journal of Petrology* **44**, 2203–2241.

Prouteau, G., Scaillet, B., Pichavant, M. & Maury, R. C. (1999). Fluid-present melting of ocean crust in subduction zones. *Geology* **27**, 1111–1114.

Ramos, V. A. (1999). Plate tectonic setting of the Andean Cordillera. *Episodes* **22**, 183–190.

Ramos, V. A., Cegarra, M. & Cristallini, E. (1996). Cenozoic tectonics of the High Andes of west–central Argentina (30–36°S latitude). *Tectonophysics* **259**, 185–200.

Ranero, C. R. & Sallarès, V. (2004). Geophysical evidence for hydration of the crust and mantle of the Nazca plate during bending at the north Chile trench. *Geology* **32**, 549–552.

Ranero, C. R., Phipps Morgan, J., Mcintosh, K. & Reichert, C. (2003). Bending-related faulting and mantle serpentinization at the Middle America trench. *Nature* **425**, 367–373.

Rapp, R. & Watson, B. (1995). Dehydration melting of metabasalt at 8–32 kbar: implication for continental growth and crust–mantle recycling. *Journal of Petrology* **36**, 891–931.

Rodríguez, C. (2006). Intra-crustal origin of Holocene adakitic magmas at Nevado de Longaví Volcano (Chile, Southern Volcanic Zone: 36·2°S). Ph.D. thesis, Université de Genève, 120 pp.

Roeder, P. L. & Emslie, R. F. (1970). Olivine–liquid equilibrium. *Contributions to Mineralogy and Petrology* **29**, 275–289.

Rudnick, R. L. & Gao, S. (2003). Composition of the continental crust. In: Rudnick, R. L. (ed.) *The Crust*. Oxford: Pergamon, pp. 1–64.

Rutherford, M. J. & Devine, J. D. (1988). The May 18, 1980, eruption of Mount St. Helens, 3. Stability and chemistry of amphibole in the magma chamber. *Journal of Geophysical Research* **93**, 11949–11959.

Rutherford, M. & Devine, J. (1996). Preeruption pressure–temperature conditions and volatiles in the 1991 dacitic magma of Mount Pinatubo. In: Newhall, C. G. & Punongbayan, R. S. (eds)

Fire and Mud: Eruptions and Lahars of Mount Pinatubo, Philippines. Seattle; Quezon City, Philippines: PHIVOLCS, pp. 751–766.

Rutherford, M. & Hill, P. (1993). Magma ascent rates from amphibole breakdown: an experimental study applied to the 1980–1986 Mount St. Helens eruption. *Journal of Geophysical Research* **98**, 19667–19685.

Sack, R. & Ghiorso, M. (1991). Chromian spinels as petrogenetic indicators: thermodynamics and petrological applications. *American Mineralogist* **76**, 827–847.

Sajona, F. G., Maury, R. C., Bellon, H., Cotten, J., Defant, M. J. & Pubellier, M. (1993). Initiation of subduction and the generation of slab melts in western and eastern Mindanao, Philippines. *Geology* **21**, 1007–1010.

Scaillet, B. & Evans, B. (1999). The June 15, 1991 eruption of Mount Pinatubo. I. Phase equilibria and pre-eruption of P–T–fO_2–H_2O conditions of the dacite magma. *Journal of Petrology* **40**, 381–411.

Schnetzler, C. C. & Philpotts, J. A. (1970). Partition coefficients of rare-earth elements between igneous matrix material and rock-forming mineral phenocrysts—II. *Geochimica et Cosmochimica Acta* **34**, 331–340.

Sellés, D. (2006). Stratigraphy, petrology, and geochemistry of Nevado de Longaví volcano, Chilean Andes (36·2°S). Ph.D. thesis, Université de Genève, 103 pp.

Sellés, D., Rodríguez, C., Dungan, M. A., Naranjo, J. & Gardeweg, M. (2004). Geochemistry of Nevado de Longaví volcano (36·2°S): A compositionally atypical arc volcano in the Southern Volcanic Zone of the Andes. *Revista Geológica de Chile* **31**, 293–315.

Sisson, T. W. & Grove, T. L. (1993). Experimental investigations of the role of H_2O in calc-alkaline differentiation and subduction zone magmatism. *Contributions to Mineralogy and Petrology* **113**, 143–166.

Solidum, R. U., Castillo, P. R. & Hawkins, J. W. (2003). Geochemistry of lavas from Negros Arc, west central Philippines: Insights into the contribution from the subducting slab. *Geochemistry, Geophysics, Geosystems* **4**, 9008doi:9010.1029/2003GC000513.

Sruoga, P., Llambías, E. J., Fauqué, L., Schonwandt, D. & Repol, D. G. (2005). Volcanological and geochemical evolution of the Diamante Caldera–Maipo volcano complex in the Southern Andes of Argentina (34°10'S). *Journal of South American Earth Sciences* **19**, 399–414.

Stern, C. R. (1991). Role of subduction erosion in the generation of Andean magmas. *Geology* **19**, 78–81.

Stern, C. R. & Kilian, R. (1996). Role of the subducted slab, mantle wedge and continental crust in the generation of adakites from the Andean Austral Volcanic Zone. *Contributions to Mineralogy and Petrology* **123**, 263–281.

Stormer, J. (1983). The effects of recalculation on estimates of temperature and oxygen fugacity from analyses of multicomponent iron–titanium oxides. *American Mineralogist* **68**, 586–594.

Tagiri, M., Moreno, H., López-Escobar, L. & Notsu, K. (1993). Two magma types of the high-alumina basalt series of Osorno volcano, southern Andes (41°06'S)—plagioclase dilution effect. *Journal of Mineralogy, Petrology and Economic Geology* **88**, 359–371.

Takagi, D., Sato, H. & Nakagawa, M. (2005). Experimental study of a low-alkali tholeiite at 1–5 kbar: optimal condition for the crystallization of high-An plagioclase in hydrous arc tholeiite. *Contributions to Mineralogy and Petrology* **149**, 527–540.

Tassara, A. (2005). Structure of the Andean continental margin and causes of its segmentation. Ph.D. thesis, Freie Universität Berlin, 181 pp.

Tassara, A. & Yañez, G. (2003). Relación entre el espesor elástico de la litosfera y la segmentación tectónica del margen andino (15–47°S). *Revista Geológica de Chile* **30**, 159–186.

Tebbens, S. & Cande, S. (1997). Southeast Pacific tectonic evolution from early Oligocene to Present. *Journal of Geophysical Research* **102**, 12061–12084.

Thorkelson, D. J. & Breitsprecher, K. (2005). Partial melting of slab window margins: genesis of adakitic and non-adakitic magmas. *Lithos* **79**, 25–41.

Tormey, D., Hickey-Vargas, R., Frey, F. & López-Escobar, L. (1991). Recent lavas from the Andean volcanic front (33 to 42°S); interpretations of along-arc compositional features. In: (Harmon, R. S. & Rapela, C. W. (eds) *Andean Magmatism and its Tectonic Setting. Geological Society of America, Special Papers* **265**, 57–77.

Tormey, D., Frey, F. & López-Escobar, L. (1995). Geochemistry of the active Azufre–Planchón–Peteroa Volcanic Complex, Chile (35°15'S): Evidence for multiple sources and processes in a Cordilleran arc magmatic system. *Journal of Petrology* **36**, 265–298.

Ulmer, P. (1989). The dependence of the Fe^{2+}–Mg cation-partitioning between olivine and basaltic liquid on pressure, temperature and composition. *Contributions to Mineralogy and Petrology* **101**, 261–273.

Ulmer, P. & Müntener, O. (2005). 'Adakites' formed by garnet fractionation at the base of the crust—an alternative scenario supported by field and experimental data. *Geophysical Research Abstracts* **7**, SRef-ID: 1607-7962/gra/EGU1605-A-09837.

Ulmer, P. & Trommsdorff, V. (1995). Serpentine stability to mantle depths and subduction-related magmatism. *Science* **268**, 858–861.

Vance, J. A. (1969). On synneusis. *Contributions to Mineralogy and Petrology* **24**, 7–29.

Watson, E. B. & Green, T. H. (1981). Apatite/liquid partition coefficients for the rare earth elements and strontium. *Earth and Planetary Science Letters* **56**, 405–421.

Yogodzinski, G. M. & Kelemen, P. B. (1998). Slab melting in the Aleutians: implications of an ion probe study of clinopyroxene in primitive adakite and basalt. *Earth and Planetary Science Letters* **158**, 53–65.

Yogodzinski, G., Lees, J., Churikova, T., Dorendorf, F., Wöerner, G. & Volynets, O. (2001). Geochemical evidence for the melting of subducting oceanic lithosphere at plate edges. *Nature* **409**, 500–504.